

# A mass and momentum flux-form high-order discontinuous Galerkin shallow water model on the cubed-sphere



Lei Bao<sup>a,\*</sup>, Ramachandran D. Nair<sup>b</sup>, Henry M. Tufo<sup>c</sup>

<sup>a</sup> Dept. of Applied Mathematics, The University of Colorado at Boulder, CO 80309, USA

<sup>b</sup> National Center for Atmospheric Research, 1 1850 Table Mesa Drive, Boulder, CO 80305, USA

<sup>c</sup> Dept. of Computer Science, The University of Colorado at Boulder, CO 80309, USA

## ARTICLE INFO

### Article history:

Received 20 May 2013

Received in revised form 17 October 2013

Accepted 24 November 2013

Available online 12 December 2013

### Keywords:

Discontinuous Galerkin  
Shallow-water equations  
Flux-form  
Bottom topography  
Cubed-sphere  
Well-balanced  
Second-order diffusion  
Conservative form

## ABSTRACT

A well-balanced discontinuous Galerkin (DG) flux-form shallow-water (SW) model on the sphere is developed and compared with a nodal DG SW model cast in the vector-invariant form for accuracy and conservation properties. A second-order diffusion scheme based on the local discontinuous Galerkin (LDG) method is added to the viscous version of the SW model and tested for conservation behaviors. The inviscid flux-form SW model is found to have better conservation of total energy and zonal angular momentum while the vector-invariant form provides better ability of conserving potential enstrophy. The inviscid flux-form tends to generate spurious vorticity but the LDG scheme combined with a well-balanced treatment can effectively eliminate the small-scale noise and generate smooth and accurate results.

© 2013 Elsevier Inc. All rights reserved.

## 1. Introduction

The shallow-water equations (SWEs) are considered to be a testbed for numerical methods for global atmospheric modeling, as they mimic their important features of the horizontal aspects of the dynamics. The SWEs describe the evolution of a homogeneous, hydrostatic, nonlinear fluid in the ocean or atmosphere on the sphere, and can be derived by vertically-integration of the Navier–Stokes equations under the assumption that the horizontal length scale is much larger than the vertical [1]. The shallow water system provides a framework to develop numerical schemes for atmospheric computation, before testing the proposed numerical approaches in a full climate model. Although numerous formulations of SWEs on the sphere are available (see, for example, [2]), we are particularly interested in the flux-form formulation which are amenable to the development of numerically conservative models. The conservative form of the equations typically refers to the *strong conservative* form, where the source terms are absent [3]. However, we use the term “flux-form” or “conservative form” interchangeably here to refer the conservative formulation with source terms.

Conservation of global integral invariants such as mass, momentum and energy is very important for climate modeling where the model may be integrated of the order of hundreds of years. In a recent review, Thuburn [4] underscores the importance of conservation in dynamical cores which are used for climate simulations. Mass is a robust invariant and should be conserved by the numerical scheme. It is well known that the total potential energy is responsible for the global mean

\* Corresponding author.

E-mail addresses: lei.bao@colorado.edu (L. Bao), rnair@ucar.edu (R.D. Nair), tufo@cs.colorado.edu (H.M. Tufo).

<sup>1</sup> The National Center for Atmospheric Research is sponsored by the National Science Foundation.

temperature, and a proper treatment of the kinetic energy is important for capturing the dynamics [4]. Vorticity is a kinetic quantity and the conservation of vorticity is particularly important for long-time scale evolutions since vorticity is associated with slow modes in the flow, and the spurious generation of vorticity tends to accumulate over long times [5]. Conservation of angular momentum is particularly important for the zonal wind strength, particularly in the case of mid-latitude jets and trade winds [4]. Angular momentum has three components: two equatorial components, and the zonal (axial) angular momentum. The zonal angular momentum of the atmosphere and its relationship with the rotating Earth have been a popular topic of meteorology since the 1950s [6]. For global SWEs, mass, total energy, potential enstrophy and zonal angular momentum are conserved quantities [2], and the choice of equation set, grid system and numerical schemes is crucial for their conservation.

Many formulations of the SWEs on a rotating sphere are available for numerical modeling [2]. This includes the 3D vector formulation of flux-form SWEs, which is a general approach, free of singularities, that can be used for various spherical mesh types as shown in [7,8]. Nevertheless, this formulation changes the dimensionality of the problem from 2D to 3D, and requires a Lagrange multiplier approach that constrains the motion to follow the sphere [9]. Because of the polar singularities associated with the regular latitude–longitude grid system, new models are being developed based on an alternative scalable spherical grid system such as the cubed-sphere [10–12] amongst other options. The cubed-sphere geometry removes these singularities and provides an alternative mesh comprised of the quasi-uniform rectangular tiling. Due to its grid structure, the cubed-sphere geometry is very popular for atmospheric model development based on numerical methods such as the element-based Galerkin methods [13,14] and various finite-volume methods [15–19].

In this paper we consider the full flux-form SWEs on the cubed-sphere. For the full flux-form SWEs, the prognostic variables (state vector) are  $[uh, vh, h]^T$ , where  $u$  and  $v$  are the wind vector components and  $h$  is the height field. For the vector-invariant form [20] the prognostic variables are  $[u, v, h]^T$ . The flux-form has an explicit rigorous treatment of momentum which leads to better momentum conservation. However, in non-orthogonal curvilinear geometry such as the cubed-sphere, the momentum equations are in tensor form consisting of several metric terms. The vector-invariant form preserves the original form, as its name implies, and is relatively easy to solve. Both formulations have their strengths and weaknesses. In this paper we make a rigorous comparison of the two by solving them using a high-order nodal Discontinuous Galerkin (DG) method on the cubed-sphere.

The discontinuous Galerkin (DG) method can be viewed as a combination of the finite-element and finite-volume methods, which retains the best features of each [21]. Due to its advantages such as data locality (parallel efficiency), high-order accuracy and geometric flexibility, it has become a method of choice for many scientific and engineering problems. Shallow water (SW) models based on a high-order DG discretization method have been developed [7,14,22], including a viscous formulation [23] for global modeling. However, when applied to SWEs, traditional DG formulations are not “well-balanced” in the presence of non-smooth bottom topography. Recently, a well-balanced DG scheme for SWEs was developed by Xing and Shu [24,25] in the 2D plane in Cartesian coordinates. Here, we extend this approach for our flux-form SW model on the cubed-sphere. We also consider a viscous formulation produced by the addition of a second-order diffusion term, using a local DG (or LDG) approach. The time integration procedure utilizes an explicit Runge–Kutta integration scheme [26]. The conservation properties of the flux-form SW model are compared with the vector-invariant form, as described in [23], using several benchmark tests [2,27].

The remainder of the paper is organized as follows. In Section 2, we briefly introduce the two forms of the shallow-water model and set up some basic notations. The discretization of the well-balanced viscous flux form of shallow-water model (based on LDG approach) is discussed in Section 3, as is its implementation on the cubed-sphere. Numerical experiments and results are discussed in Section 4. Section 5 provides the summary and conclusions.

## 2. Shallow-water equations on the rotating sphere

The system of SWEs consists of the continuity and momentum equations. The continuity equation is accountable for the conservation of mass, and is formulated as follows,

$$\frac{\partial h}{\partial t} + \nabla \cdot (h\mathbf{v}) = 0. \quad (1)$$

Usually, the momentum equations are written in vector form [2]. In the context of numerical modeling, two forms of momentum equations are widely used. They are the conservative form (2) and the vector-invariant form (3),

$$\frac{\partial h\mathbf{v}}{\partial t} + \nabla \cdot \left( h\mathbf{v}\mathbf{v} + \frac{1}{2}gh^2\mathbf{I} \right) = -f\hat{\mathbf{k}} \times h\mathbf{v} - gh\nabla h_s, \quad (2)$$

$$\frac{\partial \mathbf{v}}{\partial t} + \nabla \cdot \left( \frac{\mathbf{v} \cdot \mathbf{v}}{2} \right) = -(\zeta + f)\hat{\mathbf{k}} \cdot \mathbf{v} - \nabla\Phi. \quad (3)$$

Here,  $h$  is the depth of the fluid above the solid surface,  $h_s$  is the height of the bottom topography, which may be a river bed or an underlying mountain.  $\mathbf{v}$  is the horizontal wind vector,  $f$  is the Coriolis parameter,  $\hat{\mathbf{k}}$  is the unit vector along the outward radial direction, and  $\mathbf{I}$  is the  $2 \times 2$  identity matrix.  $\Phi = g(h_s + h)$  is the geopotential height at the free surface of the

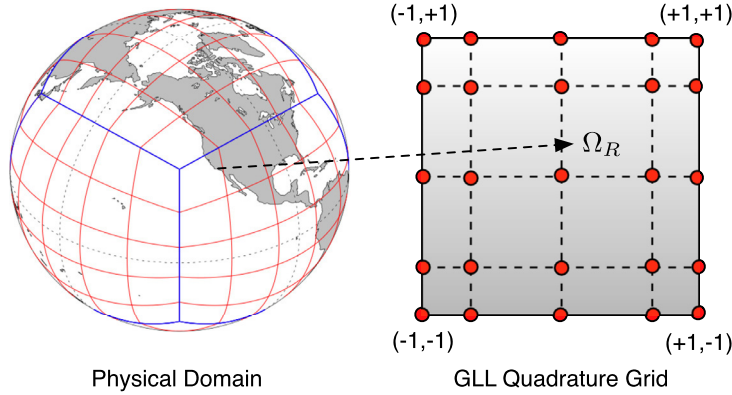


**Fig. 1.** A schematic of a cubed-sphere grid with quadrilateral elements is shown in the left panel. The right panel shows a reference element  $\Omega_e$  with  $5 \times 5$  GLL quadrature grid points. Each element  $\Omega_{ij}$  on the cube face of the physical domain is mapped onto a unique reference element  $\Omega_R$ . The mapping from the physical domain to the reference element is given in (16).

fluid (above sea level).  $\zeta = \hat{\mathbf{k}} \cdot (\nabla \times \mathbf{v})$  denotes the relative vorticity. Note that, divergence ( $\nabla \cdot$ ) and gradient ( $\nabla$ ) operators are defined in general cases. In other words, they are not specific to a particular grid system.

The flux-form of SWEs consists of (1) and (2), while the vector-invariant form of SWEs is composed of (1) and (3). In the continuous sense, both forms are mathematically equivalent for smooth waves, while in the discrete settings, they are not identical and they have their own focuses. For the flux-form, the rigorous form of momentum appears in the momentum equations. It states the conservation of momentum physically. The state variables for the momentum equations in the conservative form and the vector-invariant form are  $h\mathbf{v}$  and  $\mathbf{v}$ , respectively. The advantage of choosing  $h\mathbf{v}$  as a prognostic variable is that, if letting  $h \rightarrow 0$ , the prognostic variable goes to zero as long as  $\mathbf{v}$  stays bounded. Note that  $h \rightarrow 0$  corresponds to a massless layer in numerical modeling. By employing the conservative form of momentum equations, the discrete system is still well-behaved even we evacuate the mass of a given layer [5].

Moreover, since (3) expresses the conservation of particle velocity  $\mathbf{v}$ , which is physically meaningless, the vector-invariant form is, in some sense, mathematically conservative but not physically conservative [28]. In the presence of shock waves, the two forms can lead to two different solutions. The flux-form tends to be a better shock capturing method, whereas numerical solution from vector-invariant form will still produce shocks but with wrong propagation speed, even employing conservative numerical methods [28].

On the other hand, the vector-invariant form is a popular choice in climate modeling. It is very difficult to find the shortcomings of this form in numerical computing [5]. In addition, if we take  $\nabla \times$  of momentum equation (3), we can immediately obtain a vorticity equation while the same manipulation on (2) does not. In other words, discrete systems based on the conservative form of the momentum equation (2) do not guarantee the conservation of vorticity. Every term in (2) tends to introduce spurious vorticity into the system [5]. If no treatment is applied to suppress the noise, the flux-form may eventually produce an inaccurate and unacceptable numerical solution [5].

### 2.1. Cubed-sphere geometry

The cubed-sphere was originally introduced by Sadourny [10], and variants including equiangular projection were developed by Ronchi et al. [11] and Rančić et al. [12]. Let sphere  $\mathcal{S}$  be the physical domain, which is the surface of the planet earth. The left panel in Fig. 1 is a schematic of physical domain on a cubed-sphere grid.  $\mathcal{S}$  is partitioned into six identical patches that are obtained by the projection of the faces of an inscribed cube. In the present model, we consider the gnomonic (equiangular) central projection [10], which is non-orthogonal but more uniform than the conformal mapping [12]. The salient features of the resulting gnomonic coordinate system on  $\mathcal{S}$  are a global grid system without polar singularities, and identical metric terms on each panel with quasi-uniform grid cells [14].

We define the local equiangular coordinate system of each face as  $x^1 = x^1(\lambda, \theta)$ ,  $x^2 = x^2(\lambda, \theta)$ , where  $x^1, x^2 \in [-\pi/4, \pi/4]$  and  $\lambda, \theta$  are the longitude and latitude of a sphere with radius  $R$ . Let  $\mathbf{a}_1, \mathbf{a}_2$  be the covariant base vectors of the transformation between the inscribed cube  $\mathcal{C}$  and the spherical surface  $\mathcal{S}$ , then the corresponding transformation matrix is defined as:

$$A = \begin{bmatrix} \cos \theta \partial \lambda / \partial x^1 & \cos \theta \partial \lambda / \partial x^2 \\ \partial \theta / \partial x^1 & \partial \theta / \partial x^2 \end{bmatrix} = [\mathbf{a}_1 \quad \mathbf{a}_2].$$

The corresponding metric tensor  $G_{ij}$  is

$$G_{ij} = \frac{R^2 \sec^2 x^1 \sec^2 x^2}{1 + \tan^2 x^1 + \tan^2 x^2} \begin{pmatrix} 1 + \tan^2 x^1 & -\tan x^2 \tan x^1 \\ -\tan x^1 \tan x^2 & 1 + \tan^2 x^2 \end{pmatrix} = A^T A,$$

where  $i, j \in \{1, 2\}$ , and the Jacobian of the transformation is  $\sqrt{G} = [\det(G_{ij})]^{1/2}$ . Details of the local transformation can be found in [29], and we will not further discuss herein.

The transformation of the horizontal wind vector  $\mathbf{v} = (u, v)$  to local cubed-sphere contravariant components  $(u^1, u^2)$  and covariant components  $(u_1, u_2)$ , respectively, can be written as:

$$\begin{bmatrix} u \\ v \end{bmatrix} = A \begin{bmatrix} u^1 \\ u^2 \end{bmatrix}, \quad A^T \begin{bmatrix} u \\ v \end{bmatrix} = \begin{bmatrix} u_1 \\ u_2 \end{bmatrix},$$

and the covariant components and contravariant components are related via  $u_i = G_{ij}u^j$ ,  $u^i = G^{ij}u_j$ , and  $G^{ij} = G_{ij}^{-1}$ .

## 2.2. SWEs on the cubed-sphere

Two forms of SWEs on the cubed-sphere are expressed in the curvilinear equiangular  $(x^1, x^2)$  coordinate system.

### 2.2.1. Flux-form of SWEs on the cubed-sphere

In the curvilinear coordinates generated by cubed-sphere geometry, the flux-form of SWEs can be written in terms of contravariant components [15] as follows,

$$\frac{\partial}{\partial t} \begin{bmatrix} h \\ hu^1 \\ hu^2 \end{bmatrix} + \frac{1}{\sqrt{G}} \frac{\partial}{\partial x^1} \begin{bmatrix} \sqrt{G}hu^1 \\ \sqrt{G}\tau^{11} \\ \sqrt{G}\tau^{21} \end{bmatrix} + \frac{1}{\sqrt{G}} \frac{\partial}{\partial x^2} \begin{bmatrix} \sqrt{G}hu^2 \\ \sqrt{G}\tau^{12} \\ \sqrt{G}\tau^{22} \end{bmatrix} = \Phi_C + \Phi_T + \begin{bmatrix} 0 \\ -\Gamma_{ij}^1 \tau^{ji} \\ -\Gamma_{ij}^2 \tau^{ji} \end{bmatrix} \tag{4}$$

where the tensor  $\tau^{ij} = hu^i u^j + 1/2gh^2 G^{ij}$ , with  $i, j, k \in \{1, 2\}$ .

The last term on the right-hand side of (4) can be viewed as the source term due to the curvature of the chosen coordinate system. Here, the Christoffel symbols  $\Gamma_{ij}^k$  are needed to define the differential operators of contravariant vectors in curvilinear coordinates [30,15], noting that under the gnomonic mapping  $G^{ij}\Gamma_{ij}^k = 0$  [17]:

$$\begin{aligned} \Gamma_{11}^1 &= \frac{2 \tan x^1 \tan^2 x^2}{1 + \tan^2 x^1 + \tan^2 x^2}, & \Gamma_{12}^1 &= -\frac{\tan x^2 \sec^2 x^2}{1 + \tan^2 x^1 + \tan^2 x^2}, & \Gamma_{22}^1 &= 0, \\ \Gamma_{22}^2 &= \frac{2 \tan^2 x^1 \tan x^2}{1 + \tan^2 x^1 + \tan^2 x^2}, & \Gamma_{12}^2 &= -\frac{\tan x^1 \sec^2 x^1}{1 + \tan^2 x^1 + \tan^2 x^2}, & \Gamma_{11}^2 &= 0. \end{aligned}$$

$\Phi_C$  and  $\Phi_T$  denote the source term due to Coriolis force and the source term due to bottom topography, respectively,

$$\Phi_C = - \begin{bmatrix} 0 \\ f\sqrt{G}(G^{12}hu^1 - G^{11}hu^2) \\ f\sqrt{G}(G^{22}hu^1 - G^{12}hu^2) \end{bmatrix}, \tag{5}$$

$$\Phi_T = - \begin{bmatrix} 0 \\ gh(G^{11} \frac{\partial h_s}{\partial x^1} + G^{12} \frac{\partial h_s}{\partial x^2}) \\ gh(G^{12} \frac{\partial h_s}{\partial x^1} + G^{22} \frac{\partial h_s}{\partial x^2}) \end{bmatrix}. \tag{6}$$

### 2.2.2. Vector-invariant form of SWEs on the cubed-sphere

The vector-invariant form of SWEs is cast in terms of covariant components, which is in the following simple form [14],

$$\frac{\partial}{\partial t} \begin{bmatrix} \sqrt{G}h \\ u_1 \\ u_2 \end{bmatrix} + \frac{\partial}{\partial x^1} \begin{bmatrix} \sqrt{G}hu^1 \\ E \\ 0 \end{bmatrix} + \frac{\partial}{\partial x^2} \begin{bmatrix} \sqrt{G}hu^2 \\ 0 \\ E \end{bmatrix} = \begin{bmatrix} 0 \\ \sqrt{G}u^2(f + \zeta) \\ -\sqrt{G}u^1(f + \zeta) \end{bmatrix}. \tag{7}$$

The energy term  $E$  and relative vorticity  $\zeta$  on  $\mathcal{S}$  are defined as

$$E = \Phi + \frac{1}{2}(u_1 u^1 + u_2 u^2), \tag{8}$$

$$\zeta = \frac{1}{\sqrt{G}} \left[ \frac{\partial u_2}{\partial x^1} - \frac{\partial u_1}{\partial x^2} \right]. \tag{9}$$

Note that for the vector-invariant form, the fluxes used are the energy fluxes not the momentum fluxes.

Both (4) and (7) can be generalized in the following compact form:

$$\frac{\partial}{\partial t} \mathbf{U} + \frac{\partial}{\partial x^1} \mathbf{F}_1(\mathbf{U}) + \frac{\partial}{\partial x^2} \mathbf{F}_2(\mathbf{U}) = \mathbf{S}(\mathbf{U}). \tag{10}$$

### 3. Nodal discontinuous Galerkin discretization

Implementation of nodal DG discretization of (10) follows the same idea of [23].

#### 3.1. DG discretization

Let the computational domain  $\mathcal{D}$  be the surface of the inscribed (logical) cube  $\mathcal{C}$ , which consists of six identical non-overlapping patches, i.e.  $\mathcal{D} = \bigcup_{p=1}^6 \Omega^p$ . The discretization for each patch is identical and thus we only consider the discretization for a single face, denoted by  $\Omega$ . The square subdomain  $\Omega$  is divided into  $N_e \times N_e$  non-overlapping rectangular elements  $\Omega_{ij}$  such that,

$$\Omega_{ij} = [(x^1, x^2) | x^1 \in (x_{i-1/2}^1, x_{i+1/2}^1), x^2 \in (x_{j-1/2}^2, x_{j+1/2}^2)], \quad \text{where } i, j = 1, 2, \dots, N_e.$$

So,  $M = 6N_e^2$  elements in total which span the whole spherical domain  $\mathcal{S}$ .

DG discretization to a scalar component of (10) is illustrated here for the purpose of simplicity:

$$\frac{\partial}{\partial t} U + \nabla \cdot \mathbf{F}(U) = S(U), \quad \text{in } \mathcal{D} \times (0, T], \tag{11}$$

where  $U$  is a scalar variable, which may include the metric term  $\sqrt{G}$ ,  $\mathbf{F} = (F_1, F_2)$  is the flux function,  $S(U)$  is the source term,  $T$  is the total time period, and  $\nabla = (\partial/\partial x^1, \partial/\partial x^2)$  is the Cartesian-like gradient operator [29].

In a DG method, we solve for an approximate solution  $U_h$ , which belongs to a finite-dimensional space  $\mathcal{V}_h$  consisting of polynomials of degree up to  $N$ :

$$\mathcal{V}_h = \mathcal{V}_h^N = \{ \varphi : \varphi|_{\Omega_e} \in P^N(\Omega_e), \forall \Omega_e \in \mathcal{D} \}, \tag{12}$$

where

$$P^N(\Omega) = \text{span}\{ (x^1)^k (x^2)^l : 0 \leq k, l \leq N, \forall (x^1, x^2) \in \Omega \}.$$

The semidiscretized weak formulation for (11) on each element  $\Omega_e$  is given by [21]:

$$\frac{d}{dt} \int_{\Omega_e} U_h \varphi_h d\Omega - \int_{\Omega_e} \mathbf{F}(U_h) \cdot \nabla \varphi_h d\Omega + \int_{\Gamma_e} \hat{\mathbf{F}} \cdot \mathbf{n} \varphi_h d\Gamma = \int_{\Omega_e} S(U_h) \varphi_h d\Omega, \tag{13}$$

where  $\varphi_h$  is a test function from test space  $\mathcal{V}_h$ ,  $\hat{\mathbf{F}}$  is the numerical flux as defined below and  $\mathbf{n}$  is the outward unit normal vector along the element boundary  $\Gamma_e$ .

For simplicity, we choose Lax–Friedrichs numerical flux here:

$$\hat{\mathbf{F}}(U_h) = \frac{1}{2} \{ [\mathbf{F}(U_h^-) + \mathbf{F}(U_h^+)] \cdot \mathbf{n} - \alpha (U_h^+ - U_h^-) \}, \tag{14}$$

where  $U_h^-$  and  $U_h^+$  are the left and right limits of  $U_h$  evaluated along  $\Gamma_e$  such that  $U_h^-$  is inside the element  $\Omega_e$  and  $U_h^+$  is outside of  $\Omega_e$ ,  $\alpha$  is the maximum of the absolute value of eigenvalues of the flux Jacobian in the direction  $\mathbf{n}$ .  $\alpha$  is identical for both flux-form and vector-invariant form of SWEs. The formulations of  $\alpha$  in  $x^1$  and  $x^2$  directions are given by (detailed derivation can be found in [14]),

$$\begin{aligned} \alpha|_{x^1} &= \max\{ |u^1| + \sqrt{G^{11}gh} \}, \\ \alpha|_{x^2} &= \max\{ |u^2| + \sqrt{G^{22}gh} \}. \end{aligned} \tag{15}$$

The choice of a suitable set of basis functions for  $\mathcal{V}_h$  is also vital for an accurate and efficient evaluation of the integrals in the weak form (13). An orthogonal polynomial basis set, such as Lagrange–Legendre polynomial, is highly preferred for efficiency. Levy et al. [31] has shown that the nodal DG exhibits better computational efficiency than the modal version, therefore, we consider the nodal DG version in the present paper.

#### 3.2. Numerical integration

To make use of an efficient quadrature rule, consider a one-to-one mapping (16) from an element  $\Omega_{ij}$  to a reference element  $\Omega_R = [-1, 1] \times [-1, 1]$ , as shown in Fig. 1:

$$\begin{aligned} \xi^1 &= \frac{2(x^1 - x_i^1)}{\Delta x_i^1}, & x_i^1 &= (x_{i+1/2}^1 + x_{i-1/2}^1)/2, \\ \xi^2 &= \frac{2(x^2 - x_j^2)}{\Delta x_j^2}, & x_j^2 &= (x_{j+1/2}^2 + x_{j-1/2}^2)/2, \end{aligned} \tag{16}$$

where  $(\xi^1, \xi^2) \in \Omega_R$ . The nodal basis functions are chosen as the Lagrange–Legendre polynomials  $\phi_m(\xi^i)$ , with roots located at the Gauss–Legendre–Lobatto (GLL) quadrature points,

$$\phi_m(\xi^i) = \frac{(\xi^i - 1)(\xi^i + 1)L'_N(\xi^i)}{N(N + 1)L_N(\xi_m^i)(\xi^i - \xi_m^i)}, \tag{17}$$

$$\int_{-1}^1 \phi_m(\xi^i)\phi_n(\xi^i) d\xi^i \simeq w_m\delta_{mn}, \quad 0 \leq m, n \leq N, \tag{18}$$

where  $L_N$  is the  $N$ -th order Legendre polynomial,  $w_k$  is the weight associated with GLL quadrature rule and  $\delta_{mn}$  is the Kronecker delta function.

The tensor-product of polynomials  $\phi_m(\xi^1)\phi_n(\xi^2)$  forms the nodal basis set which spans  $P^N(\Omega_e)$  in (12). Hence, the approximate solution  $U_h$  can be expressed as the linear combination of the nodal basis set:

$$U_h(\xi^1, \xi^2) = \sum_{m=0}^N \sum_{n=0}^N U_h(\xi_m^1, \xi_n^2)\phi_m(\xi^1)\phi_n(\xi^2), \tag{19}$$

where  $\{\xi_m^i\}_{m=0}^N$  are  $N_v = N + 1$  GLL quadrature points for  $i \in \{1, 2\}$ . There are  $N_v \times N_v$  GLL points on  $\Omega_R$ , and the total degrees of freedom on  $\mathcal{D}$  are  $6N_e^2N_v^2$  with this configuration.

The bottom topography function  $h_s$  is also projected into the same space  $\mathcal{V}_h$  and is defined to be

$$h_s(\xi^1, \xi^2) = \sum_{m=0}^N \sum_{n=0}^N h_s(\xi_m^1, \xi_n^2)\phi_m(\xi^1)\phi_n(\xi^2). \tag{20}$$

The discretization of the source term bottom topography  $\Phi_T$  requires special treatment and is discussed in Section 3.4 in detail.

The same order of quadrature rule is adopted both for the internal surface integrals in  $\Omega_e$  and for the boundary flux integrals along the boundary  $\Gamma_e$ . Because, this setting is significantly efficient at the cost of negligible inaccuracy due to the inexact integration [23]. Substituting (17), (19) and (20) into the weak formulation (13) and simplifying the resulting equation lead to an ODE system in time,

$$\frac{dU_{mn}}{dt} = L(U_{mn}), \quad \text{in } (0, T], \tag{21}$$

where  $\{U_{mn}\}$  are time-dependent values of  $U_h$  at the grid points  $(x_m^1, x_n^2)$ .

### 3.3. Time integration

Strong stability-preserving (SSP) Runge–Kutta schemes are widely used in practice because they preserve stability and are flexible to increase temporal accuracy [26]. We employ a third-order accurate SSP Runge–Kutta scheme for the time integration in the present paper:

$$\begin{aligned} U^{(1)} &= U^n + \Delta tL(U^n), \\ U^{(2)} &= \frac{3}{4}U^n + \frac{1}{4}[U^{(1)} + \Delta tL(U^{(1)})], \\ U^{n+1} &= \frac{1}{3}U^n + \frac{2}{3}[U^{(2)} + \Delta tL(U^{(2)})]. \end{aligned} \tag{22}$$

Although efficient time stepping schemes, such as the implicit and semi-implicit time integration approaches, are available for DG methods, for simplicity, we consider only explicit SSP-RK method. The explicit time stepping method has a stringent CFL stability restriction for the DG methods, nevertheless, it offers high-order temporal accuracy. Note that, we use relatively small time steps for the numerical experiments for minimizing the possible temporal error associated with the numerical integration. However, for practical applications employing high-order DG methods, this may be suboptimal or computationally prohibitive.

Slope limiter procedure is an important component for many DG schemes, and a filter is also widely chosen for high-order DG schemes (see for example [7]). Because the solution contains no strong shocks or discontinuities, we adopt (22) directly without a limiter or filter.

### 3.4. Discretization of source term due to bottom topography

Bermudez and Vazquez [32] proposed the idea of the “exact C-property”, which stands for the ability of the numerical scheme to exactly preserve the steady-state equilibrium solution for the still water at rest:

$$\mathbf{v} = 0, \quad \text{and} \quad H = h + h_s = \text{constant}. \tag{23}$$

The numerical approaches which satisfy “exact C-property” are often referred as the well-balanced methods. When a non-smooth bottom topography is present in the flux-form of SWEs (4), the spatial discretization must obey the well-balanced property to avoid spurious oscillations into the flow near the non-smooth region of the bottom topography. For non-smoothness, we refer to non-differentiable function, which can also be discontinuous. The traditional DG method (13) is well-balanced for smooth bottom topography but not for the non-smooth bottom topography [24]. Well-balanced DG schemes for the SWEs are an active research area and a detailed discussion can be found in [33]. As observed in [24], a small modification on the flux term can make the traditional DG scheme well-balanced. Inspired by [24,25], we consider a well-balanced DG scheme for our flux-form SW model with a minor change in the flux term.

We define the numerical flux as  $\tilde{\mathbf{F}}(\mathbf{U}_h)$ , and the modification in the flux term is carried out in the following steps:

- After computing the boundary value of  $U_h|_{\Gamma_e}$ , define:

$$h^{*,\pm}|_{\Gamma_e} = H^\pm|_{\Gamma_e} - \max(h_s^+|_{\Gamma_e}, h_s^-|_{\Gamma_e}). \tag{24}$$

- Modify the prognostic variable  $\mathbf{U}$  along the boundary  $\Gamma_e$ :

$$U_h^{*,\pm}|_{\Gamma_e} = \begin{bmatrix} h^{*,\pm} \\ h^{*,\pm} u^{1,\pm} \\ h^{*,\pm} u^{2,\pm} \end{bmatrix}_{\Gamma_e}. \tag{25}$$

- Define the notations:

$$\delta_{x^1}^* = \begin{bmatrix} 0 \\ G^{11}[\frac{g}{2}(h^-)^2 - \frac{g}{2}(h^{*,-})^2] \\ G^{21}[\frac{g}{2}(h^-)^2 - \frac{g}{2}(h^{*,-})^2] \end{bmatrix}_{\Gamma_e}, \quad \delta_{x^2}^* = \begin{bmatrix} 0 \\ G^{12}[\frac{g}{2}(h^-)^2 - \frac{g}{2}(h^{*,-})^2] \\ G^{22}[\frac{g}{2}(h^-)^2 - \frac{g}{2}(h^{*,-})^2] \end{bmatrix}_{\Gamma_e},$$

where  $\delta_{x^1}^*$  and  $\delta_{x^2}^*$  may be interpreted as the hydrostatic reconstruction under the curvilinear coordinate system. Thus, we give the new well-balanced numerical flux:

$$\tilde{\mathbf{F}}(U_h) = \hat{\mathbf{F}}(U_h^*) + \boldsymbol{\delta} \cdot \mathbf{n}, \tag{26}$$

where  $\boldsymbol{\delta} = (\delta_{x^1}^*, \delta_{x^2}^*)$ . As shown in [24], (13) is  $(N + 1)$ -order convergence in space and converges to the weak solution.

In order to capture the non-smoothness of the bottom topography in the simulation, the initial solution is computed from the modal expression of  $h_s$  at the  $N_v \times N_v$  Gauss–Legendre (GL) points, and then interpolating it on to the corresponding GLL points. In the interpolation process, we only keep the 0-th order term, and the higher order terms are dropped in the GL quadrature.

Note that, if the bottom topography is flat or smooth, the well-balanced numerical flux is equivalent to the original numerical flux. In other words, for smooth bottom topography, the traditional DG scheme is already well-balanced. The well-balanced correction in the flux term only takes effect when there is a non-smooth bottom topography [24].

### 3.5. Artificial diffusion effects

As discussed in Section 2, the conservative form of the momentum equation (2) tends to generate noise in the vorticity field and thus destroy the conservation of potential vorticity and enstrophy as well. In order to suppress these spurious accumulation, horizontal diffusion is usually preferred and added in the discrete model [23]. In [23], the LDG approach [34] is implemented for the vector-invariant form of SWEs (7), where the LDG scheme used is based on a simple Bassi–Rebay scheme [35]. In [23], a second-order explicit diffusion ( $\nabla^2$ ) is added to (7) and tested on a series of canonical numerical test-cases for SWEs. An LDG scheme successfully removes small-scale noise and provides smooth simulated results comparable to the reference solution [23]. Similar to the idea of [23], we introduce a uniform second-order diffusion to the flux form of SWEs. The viscous SW model can be written in a compact form as follows:

$$\frac{\partial}{\partial t} \mathbf{U} + \nabla \cdot \mathbf{F}(\mathbf{U}) = \mathbf{S}(\mathbf{U}) + \mathbf{D}(\mathbf{U}). \tag{27}$$

The viscous flux  $\mathbf{D}(\mathbf{U})$  is expressed as:

$$\mathbf{D}(\mathbf{U}) = \begin{bmatrix} 0 \\ \nu\sqrt{G}\nabla_s \cdot (h\nabla_s u^1) \\ \nu\sqrt{G}\nabla_s \cdot (h\nabla_s u^2) \end{bmatrix},$$

where  $\nabla_s = (\mathbf{a}^1\partial/\partial x^1, \mathbf{a}^2\partial/\partial x^2)$ .

$$\sqrt{G}\nabla_s \cdot (h\nabla_s u^i) = \frac{\partial}{\partial x^1} \left[ h\sqrt{G}G^{11} \frac{\partial u^i}{\partial x^1} + h\sqrt{G}G^{12} \frac{\partial u^i}{\partial x^2} \right] + \frac{\partial}{\partial x^2} \left[ h\sqrt{G}G^{21} \frac{\partial u^i}{\partial x^1} + h\sqrt{G}G^{22} \frac{\partial u^i}{\partial x^2} \right],$$

where  $i \in \{1, 2\}$ , and  $\nu$  is the constant diffusion coefficient.

Note that, in the curvilinear coordinates, the vector Laplacian has a different formulation from the Laplacian of the components. Curvilinear vector Laplacian has a complex form and is computationally expensive. However, for simplicity, the Laplacian is treated component-wise for each momentum equation.

Consider the scalar component of (27),

$$\frac{\partial}{\partial t} U + \nabla \cdot \mathbf{F}(U) = S(U) + D(U). \tag{28}$$

Introduce a new variable  $\mathbf{q} = \nabla U$ , and use the following matrix notations to represent the viscous term:

$$\mathbf{q} = \left[ \frac{\partial U}{\partial x^1}, \frac{\partial U}{\partial x^2} \right], \quad \mathbf{M} = \begin{bmatrix} \sqrt{G}G^{11} & \sqrt{G}G^{12} \\ \sqrt{G}G^{21} & \sqrt{G}G^{22} \end{bmatrix}, \quad \text{and} \quad \tilde{\mathbf{q}} = h\mathbf{q}\mathbf{M}^T.$$

(28) can then be recast in the form of a first-order system on  $\mathcal{D}$ :

$$\mathbf{q} - \nabla U = 0, \tag{29}$$

$$\tilde{\mathbf{q}} = h\mathbf{q}\mathbf{M}^T, \tag{30}$$

$$\frac{\partial U}{\partial t} + \nabla \cdot \mathbf{F}(U) - \nu \nabla \cdot \tilde{\mathbf{q}} = S(U). \tag{31}$$

On each element  $\Omega_e$  with the boundary  $\Gamma_e$ , multiplying (29) by a vector test function  $\mathbf{w}$ , applying Green’s method twice, and with the central flux for the evaluation of the flux associated with  $U_h$  along  $\Gamma_e$  (see (13)–(14) in [23] for details), the weak formulation of (29) leads to:

$$\int_{\Omega_e} \mathbf{q}_h \cdot \mathbf{w} d\Omega = \int_{\Gamma_e} \frac{1}{2} (U_h^+ - U_h^-) \mathbf{w} \cdot \mathbf{n} d\Gamma + \int_{\Omega_e} \nabla U_h \cdot \mathbf{w} d\Omega, \tag{32}$$

where  $\frac{1}{2}(U_h^+ - U_h^-)$  is called jump flux.

The semidiscretized weak formulation of (31), with  $\tilde{\mathbf{q}}_h = h\mathbf{q}_h\mathbf{M}^T$ , takes the form:

$$\begin{aligned} & \frac{d}{dt} \int_{\Omega_e} U_h \varphi_h d\Omega - \int_{\Omega_e} \mathbf{F}(U_h) \cdot \nabla \varphi_h d\Omega + \int_{\Gamma_e} [\mathbf{F}(U_h)] \cdot \mathbf{n} \varphi_h d\Gamma + \nu \left( \int_{\Omega_e} \tilde{\mathbf{q}}_h \cdot \nabla \varphi_h d\Omega - \int_{\Gamma_e} [\tilde{\mathbf{q}}_h] \cdot \mathbf{n} \varphi_h d\Gamma \right) \\ & = \int_{\Omega_e} S(U_h) \varphi_h d\Omega, \end{aligned} \tag{33}$$

where  $[\tilde{\mathbf{q}}_h]$  is evaluated through the central flux  $(\tilde{\mathbf{q}}_h^+ + \tilde{\mathbf{q}}_h^-)/2$ .  $[\mathbf{F}(U_h)]$  is approximated by (26), which results in a well-balanced LDG scheme.

Although various options for the numerical fluxes are available as listed in [36], for simplicity [23], we choose the combination of jump flux and central flux here for the evaluation of (32) and (33).

The DG methods, like many other high-order methods, such as RBFs [37] and spectral element methods, often require an artificial diffusion effect to stabilize the fields and obtain a high-quality solution. For an artificial diffusion term (or a numerical diffusion),  $\nu$  depends not only on the problem itself but also the grid resolution  $\Delta\hat{h}$ .  $\nu$  is chosen in a way that the diffusion effect can, to some extent, eliminate the noise in the numerical solution, but not too large to destroy the physical features of the problem. Furthermore, it is required that as  $\Delta\hat{h} \rightarrow 0$ ,  $\nu \rightarrow 0$ . This is different from a physical diffusion (as in a viscous flow problem), where  $\nu$  relies entirely on the viscosity of the flow and is irrelevant of  $\Delta\hat{h}$ . In terms of the artificial diffusion, a rigorous selection of  $\nu$  can be made by studying the kinetic spectra [38], which is beyond the scope of the present study. Artificial diffusion is especially important when constructing dynamic core for atmosphere modeling [39,40]. In the current paper, we consider the influence of an artificial diffusion effect on our DG flux-form model. For a benchmark advection–diffusion problem, usually the analytic solution is available to test the convergence of the diffused solution. Unfortunately, there is no benchmark test with known analytic solution for SWEs (27) for examining the diffusion effect. Although the convergence study of DG with artificial diffusion effect can hardly be performed, a deviation of the diffused solution from the non-diffused solution can be shown by fixing  $\nu$  when varying  $\Delta\hat{h}$ . The indication of the influence of the numerical diffusion can be immediately seen, details are given in Section 4.1.2.

#### 4. Numerical experiments and results

To test the accuracy and the performance of our flux-form DG SW models (13), (33), we consider three standard test-cases here. They are the steady-state geostrophic flow, the zonal flow over an isolated mountain as suggested in Williamson et al. [2], and the barotropic instability proposed by Galewsky et al. [27]. The first two test-cases are often referred as the SW test-case 2 and 5, respectively [2]. Comparisons of two forms of inviscid DG SW models using these test-cases are shown, and the conservation of global invariants are monitored as a function of time.

In order to compare the resolution of cubed-sphere grids associated with GLL points with that of the regular latitude-longitude grid, we use an “average” resolution at the equator of the sphere [41]:

$$\text{approximate resolution} = \Delta \bar{h} = \frac{90^\circ}{N_e(N_v - 1)} = \frac{90^\circ}{N_e N}.$$

For most of the test-cases considered, the analytic solution is unknown. When the analytic solution is not available, a reference solution is chosen to be the numerical result produced by the inviscid vector-invariant SW model at the same resolution. In terms of the convergence studies of inviscid flux-form of SWEs, we measure the  $L_1$ ,  $L_2$  and  $L_\infty$  errors of the approximate solution, as suggested in [2]. For the convergence behavior, when including the diffusion effect, we use only the  $L_1$  error of the simulated solution, because the other two have similar convergence performances.

In order to monitor the numerical conservation of the global invariants, we define the normalized integral  $\bar{\Psi}(t)$  as:

$$\bar{\Psi}(t) = \frac{I_g[\Psi(\lambda, \theta, t)] - I_g[\Psi(\lambda, \theta, 0)]}{I_g[\Psi(\lambda, \theta, 0)]}, \quad (34)$$

where  $I_g$  is the global surface integral.  $I_g$  is evaluated on the cubed-sphere by GLL quadrature rule as follows:

$$I_g(\Psi(\lambda, \theta, t)) \approx \sum_{p=1}^6 \sum_{k=1}^{N_e} \sum_{l=1}^{N_e} \sum_{i=1}^{N_v} \sum_{j=1}^{N_v} \sqrt{G_{ijkl}} \Psi_p(x_{i,k,l}^1, x_{j,k,l}^2, t) w_i w_j,$$

where  $p$  indicates the panel index.

For the conservation of mass,  $\Psi = h$ , and for the conservation of total energy,  $\Psi = \{h(u^2 + v^2) + g[(h + h_s)^2 - h_s^2]\}/2$ . For the conservation of potential enstrophy,  $\Psi = (\zeta + f)^2/(2h)$ , where  $\zeta$  is defined in (9). For the conservation of zonal angular momentum,  $\Psi = (u + \omega R \cos \theta)R \cos \theta$  (for thin atmosphere [42]), where  $\omega$  is the angular velocity. Time traces of these integral invariants are shown for the comparison of different numerical experiments.

Note that, the SSP-RK time integration schemes impose a stringent CFL stability restriction for the DG discretizations. The presence of the diffusion terms further confine the explicit time-step size [23]. Besides, in order to carry out a fair comparison of the two sets of SWEs, it would be beneficial to avoid possible temporal errors. Due to these facts, we choose a moderate time stepping which is suboptimal. It is well-known that the communication expenses are the major limiting factor for parallel efficiency [31]. The extra cost of the flux calculations in the LDG scheme (28) is time-consuming and reduces the scalability [23]. We test two options: one is to update diffusion terms in every stage of SSP-RK3 (22), and the other is to compute it at the beginning of (22) and use the same value of diffusion terms for every inner stage of (22). For small  $\Delta t$ , numerical results show that there is no significant difference in the quality of solutions between these two choices, while the latter one is more efficient than the former one. We should emphasize that, the second treatment of the diffusion terms may not apply to general cases with relatively large  $\Delta t$ . The motivation for us to consider this setup is simplicity and efficiency. Therefore, in the numerical experiments, we adopt the second option for the LDG diffusion process.

The physical parameters used in the numerical tests are: radius of Earth  $R = 6.37122 \times 10^6$  m, angular velocity of Earth  $\omega = 7.292 \times 10^{-5}$  rad s<sup>-1</sup>, and gravitational acceleration  $g = 9.80616$  m s<sup>-2</sup>.

##### 4.1. Geostrophic flow

The first test is SW test-case 2, which describes a zonal geostrophic balanced flow [2]. It is a steady-state test for the global SWEs with a uniform wind field. The initial (also analytic) geopotential and the velocity are given as,

$$gh = gh_0 - \frac{u_0}{2}(2R\omega + u_0) \times (\sin \theta \cos \alpha_0 - \cos \lambda \cos \theta \sin \alpha_0)^2, \quad (35)$$

$$u = u_0(\cos \alpha_0 \cos \theta + \sin \alpha_0 \cos \lambda \sin \theta), \quad (36)$$

$$v = -u_0 \sin \alpha_0 \sin \lambda, \quad (37)$$

where  $u_0 = 2\pi R/(12 \text{ days})$ ,  $gh_0 = 2.94 \times 10^4$  m<sup>2</sup> s<sup>-2</sup> and  $\alpha_0$  is the flow orientation angle

It is a challenging test for the cubed-sphere geometry when  $\alpha_0$  is set to be  $\pi/4$ . Since the analytic solution is known, SW test-case 2 is usually used for validating the accuracy and studying the convergence of the numerical models. Williamson et al. [2] suggested at least 5 model days of time integration for this test. Therefore, SW models considered here are integrated for 5 model days with time step size  $\Delta t = 90$  s, for all the experiments, regardless of the resolution. The resolution for the calculation is chosen as  $N_e = 12$ ,  $N = 3$ , which corresponds to approximately  $2.5^\circ$  at the equator.

#### 4.1.1. DG for flux-form inviscid SWEs

The initial condition is shown in Fig. 2(a). Relative errors of the height difference field for two forms of SWEs are displayed in Fig. 2(b) and 2(c). The maximum relative errors are  $O(10^{-6})$  for both forms. As seen from Fig. 2(b) and 2(c), the height field in the vector-invariant form is less noisy than that of the flux-form.

To get the notion of the numerical convergence of our flux-form SW model (4), we organize the experiments in two ways. Firstly, we fix  $N_e = 3$  and increase the order of polynomial  $N$  from 4 to 10. The results are shown in Fig. 3(a), which shows an exponential convergence. Then, we perform an  $h$ -convergence study, by varying  $N_e$  from 5 to 15 with a fixed order of polynomial  $N = 3$ , and it is displayed in Fig. 3(b). It is observed that the nodal DG scheme attains at least 4-th order convergence. Both  $p$ -convergence and  $h$ -convergence performances are similar to those of the vector-invariant form [14].

Time traces of normalized errors of the global invariants are shown in Fig. 4. The results from the vector-invariant form are also displayed for reference and comparison. We can see that both forms preserve mass to the machine precision. The flux-form tends to have better conservation of total energy, while the vector-invariant form has a nicer control of potential enstrophy. This is consistent with the potential weakness of the flux-form of SWEs discussed in Section 2. However, for both sets of SWEs, the potential enstrophy is conserved up to a small constant at the same order.

#### 4.1.2. LDG for viscous flux-form of SWEs

As discussed in Section 3.5, a convergence study of the flux-form SWEs with artificial diffusion, namely as  $\Delta h \rightarrow 0$ ,  $\nu \rightarrow 0$ , is not feasible, given the fact that neither the analytic solution for viscous SWEs nor a rigorous choice of  $\nu$  is available. Therefore, we demonstrate the influence of the artificial diffusion by showing how the diffused solution deviates from the non-diffused solution. This is achieved by keeping  $\nu$  fixed and varying the resolution.

Fig. 5 shows the normalized  $L_1$  errors of the height field with various choices of the diffusion coefficients  $\nu$  when refining the grid resolution. Fig. 5(a) displays the  $L_1$  errors of the height field at day 5 when  $N_e = 3$ , and  $N$  varies from 4 to 10. As we increase the resolution, the non-diffused version exhibits an exponential convergence to the exact solution, while the LDG solution evolves to a “diffused state”, which depends on the magnitude of the diffusion coefficient  $\nu$ . Similar trends can be found in Fig. 5(b), which shows the normalized  $L_1$  errors of the height field at day 5 when  $N = 3$  and  $N_e$  varies from 5 to 15. The results in Fig. 5 reveal that when a stronger numerical diffusion is added, the diffused solution reaches a “diffused equilibrium” at a lower resolution. The “diffused equilibrium” corresponds to the flattened lines in Fig. 5(a). This implies that the diffusion effect becomes dominant, and as a result, the fine physical features due to the high-order nature of the solution are smeared or erased when a stronger numerical diffusion is used. Comparing Fig. 5(a) and 5(b), the magnitude of the diffusion coefficient plays a predominant role on the evolution of the viscous solution over the resolution or the polynomial degree.

To study the influence of the diffusion effect on the effectiveness of the scheme in conserving global invariants, time traces of the normalized errors are exhibited in Fig. 6. For all the global invariants considered here, the normalized errors grow at a higher rate when increasing the strength of the diffusion effect. The convergence behaviors of the viscous flux-form SWEs are similar to those of viscous vector-invariant form [23].

#### 4.2. Barotropic instability (Galewsky test)

The barotropic instability test of [27] simulates a mid-latitude jet generated by adding a small amount of perturbation to the barotropic balanced flow. This test is particularly challenging on the cubed-sphere grid, because the barotropic instability activities are presented at the discontinuous edges of the top panel of cubed-sphere grid, as observed by St-Cyr et al. [43]. A 6-day time integration is recommended for this test both for with and without diffusion. We are particularly interested in the relative vorticity field for this test-case. As shown in [43], nice features of the vorticity fields can be captured at a resolution higher than  $1.25^\circ$ .

For this experiment, we choose the grid resolution at  $N_e = 30$ ,  $N = 7$ , which is approximately  $0.43^\circ$  at the equator. We choose the time step size  $\Delta t = 5$  s for all the simulated runs, which is suboptimal, and integrate the model for 6 model days.

The relative vorticity fields at day 6 are shown in Fig. 7 for the inviscid and viscid flux-form of the SWEs. Fig. 7(a) shows the inviscid run and it can be seen that the non-diffused flux-form is able to well capture the dynamics and the solution is smooth and comparable to that in [23,27]. Usually, high-order methods, such as RBF [37], require strong diffusion to stabilize the result for this test-case. From various numerical experiments, we observe that the inviscid flux-form can produce a smooth relative vorticity field as long as the grid resolution is greater than  $0.5^\circ$ . However, the vector-invariant form without diffusion is very sensitive to the resolution parameters  $N_e$ ,  $N$ .

In order to consider the diffusion effect, Fig. 7(b), 7(c) show the viscous tests with the diffusion coefficients  $\nu$  ( $\text{m}^2 \text{s}^{-1}$ ) equals to  $10^4$  and  $10^5$  respectively. The viscid version successfully eliminates the small-scale noise appearing in Fig. 7(a) with a proper choice of diffusion coefficient value  $\nu$  (here,  $\nu = 10^4$  for instance). However, here the choice of the diffusion coefficient is heuristic, and somewhat arbitrary.

Time traces of the normalized errors of conservative integrals are shown in Fig. 8 with the diffusive effect. Similar to SW test-case 2, the error growth is at a noticeable faster rate and is strongly influenced by the magnitude of the value of  $\nu$ .

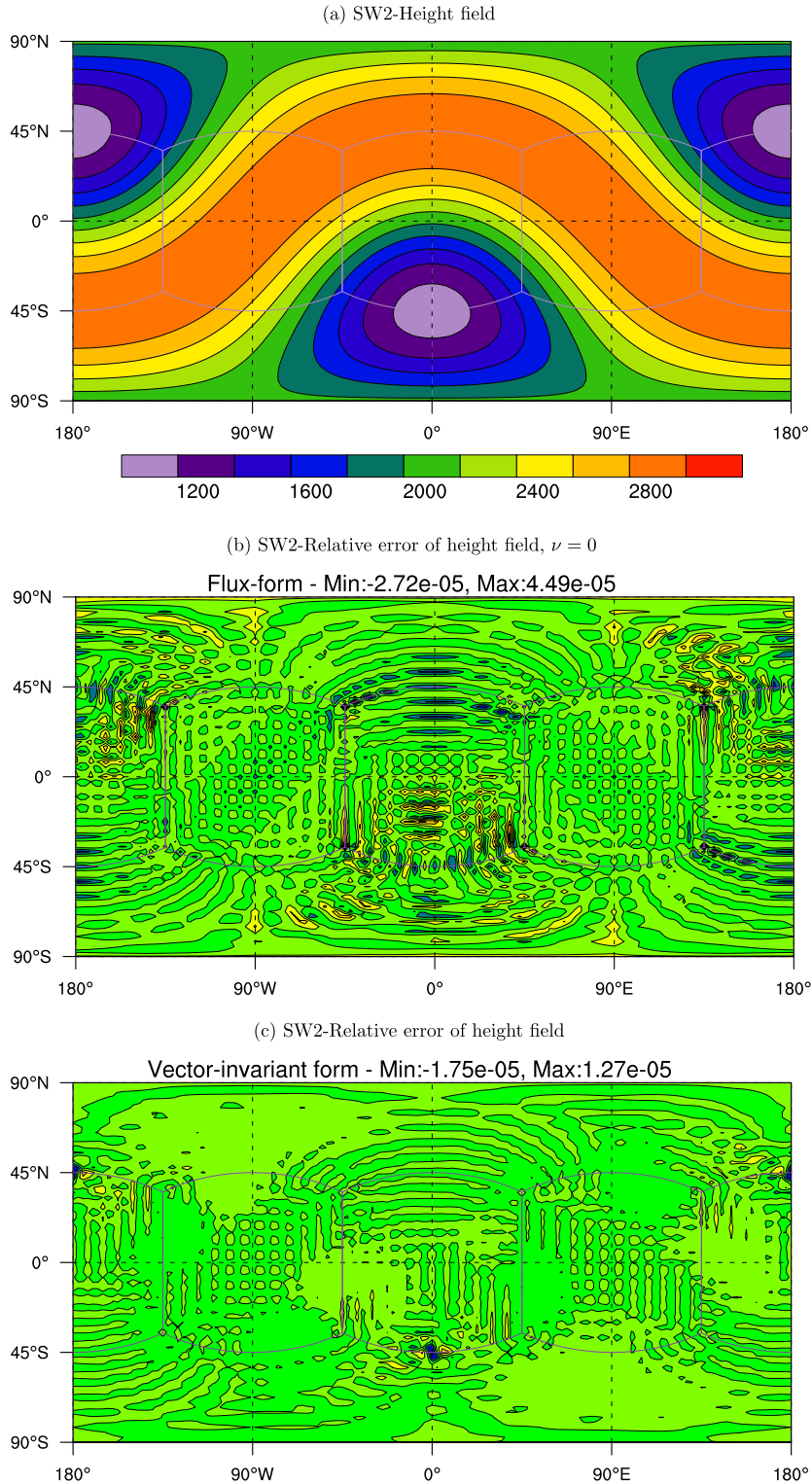


**Fig. 2.** The geostrophic flow (SW test-case 2) in the resolution  $\approx 2.5^\circ$  at the equator ( $N_e = 12, N = 3$ ) and  $\Delta t = 90$  s. (a) is the reference solution. Relative errors of height field at day 5 are shown in (b) for the flux-form of SWEs and (c) for the vector-invariant form. The contour varies from  $-3 \times 10^{-5}$  to  $4 \times 10^{-5}$  with an increment of  $5 \times 10^{-6}$ .

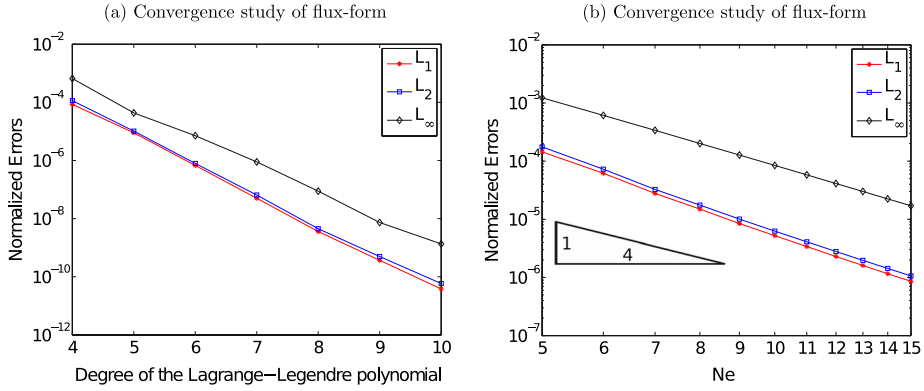


**Fig. 3.** Normalized errors of the height field for the geostrophic flow (SW test-case 2) at day 5 for the inviscid flux-form SW model. (a) is computed with  $N_e = 3$  and varying  $N$  from 4 to 10. (b) is computed with  $N = 3$  and varying  $N_e$  from 5 to 15.

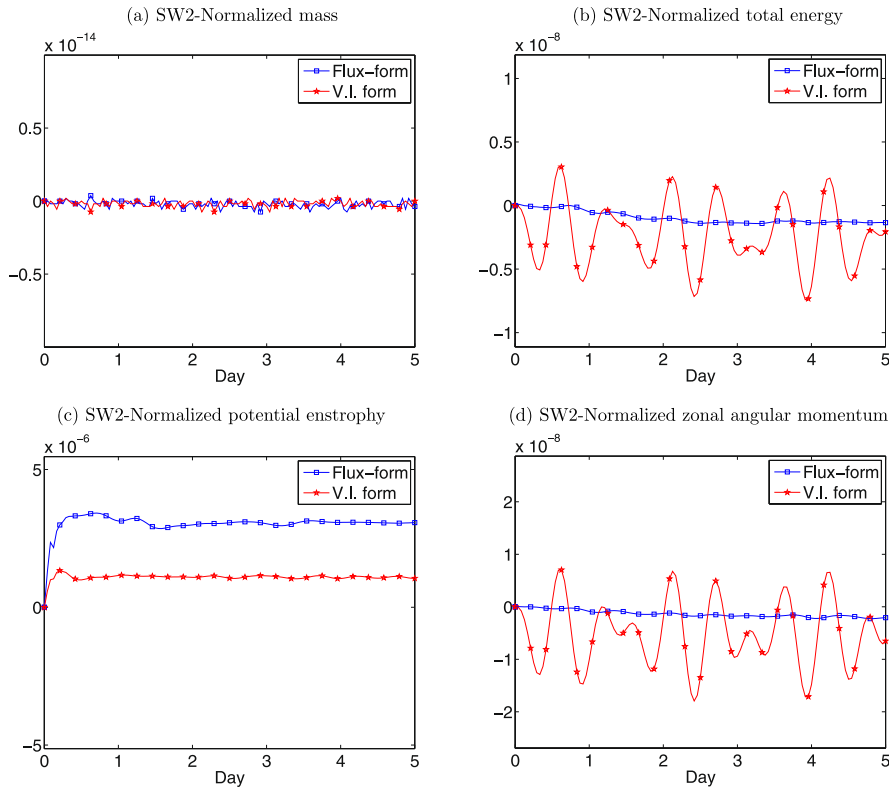


**Fig. 4.** Time traces of normalized errors of mass (a), total energy (b), potential enstrophy (c) and zonal angular momentum (d) of the flux-form and the vector-invariant form for the geostrophic flow (SW test-case 2) in the resolution  $\approx 2.5^\circ$  at the equator ( $N_e = 12, N = 3$ ). Both tests are integrated for 5 days with  $\Delta t = 90$  s.

### 4.3. Zonal flow over an isolated mountain

The last test-case we consider in this study is the SW test-case 5 in [2]. This test-case describes a zonal flow over an isolated *mountain*. It is the only test considered here in which the bottom topography is non-flat. The bottom topography is a conical mountain centered at  $(\lambda_c, \theta_c) = (3\pi/2, \pi/6)$ , which is also non-smooth. So, the well-balanced DG scheme takes effect on this test-case. The initial wind field and height field are identical to the SW test-case 2, except that  $\alpha_0 = 0, h_0 = 5960$  m and  $u_0 = 20$  m/s. The underlying mountain is defined as:

$$h_s = h_s^0 \left( 1 - \frac{r}{a} \right) \tag{38}$$

where  $h_s^0 = 2000$  m,  $a = \pi/9$ , and  $r^2 = \min[a^2, (\lambda - \lambda_c)^2 + (\theta - \theta_c)^2]$ .

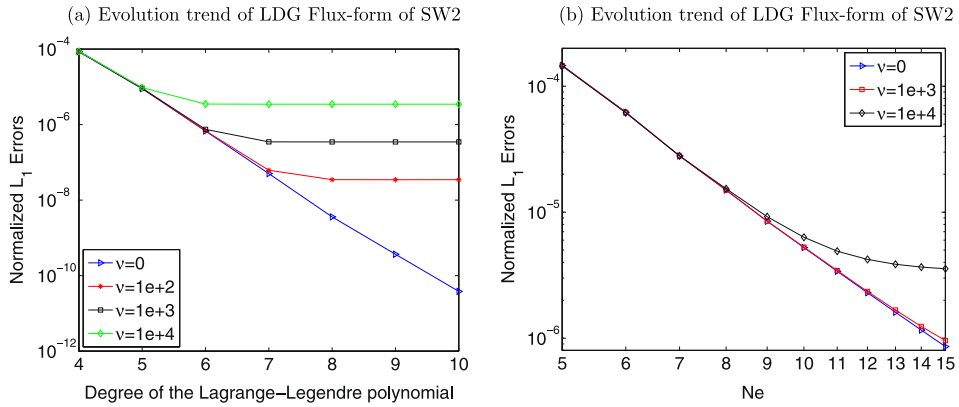


**Fig. 5.** Normalized  $L_1$  errors in the height field for SW test-case 2 at day 5 for flux-form of SWEs with diffusion for  $\nu = 0 \text{ m}^2 \text{ s}^{-1}$ ,  $\nu = 10^2 \text{ m}^2 \text{ s}^{-1}$ ,  $\nu = 10^3 \text{ m}^2 \text{ s}^{-1}$ ,  $\nu = 10^4 \text{ m}^2 \text{ s}^{-1}$  respectively. (a) is computed with  $N_e = 3$  and varying  $N$  from 4 to 10. (b) is computed with  $N = 3$  and varying  $N_e$  from 5 to 15.

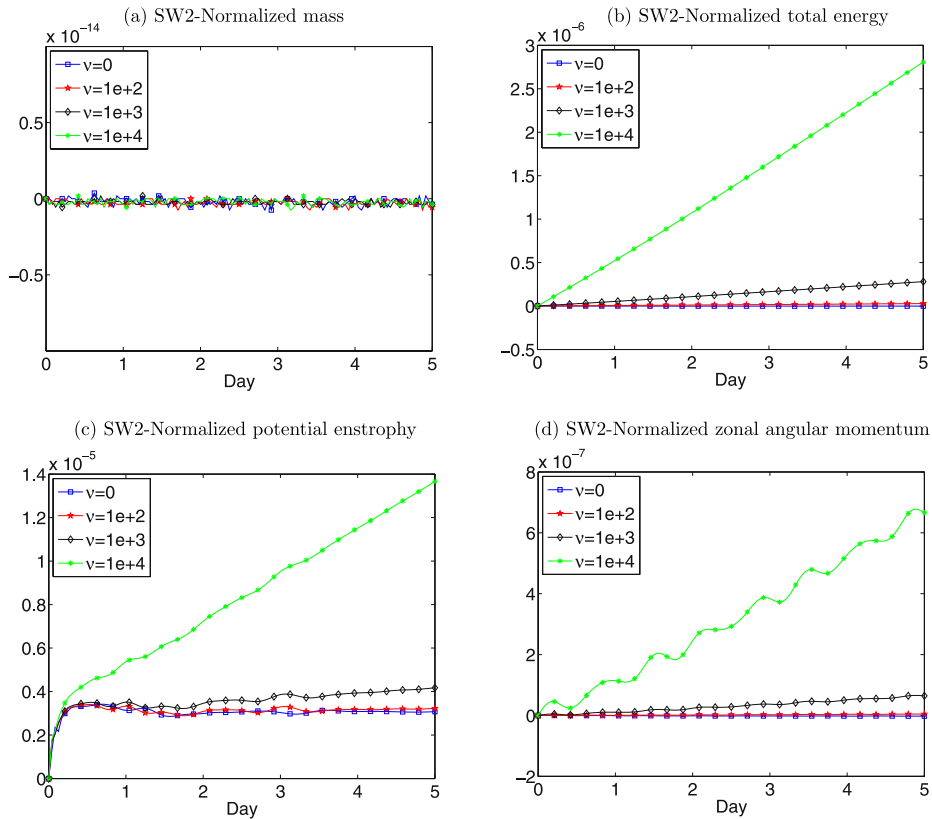


**Fig. 6.** Time traces of the normalized errors of mass (a), total energy (b), potential enstrophy (c) and zonal angular momentum (d) of viscous flux-form SWEs for the geostrophic flow (SW test-case 2) in the resolution  $\approx 2.5^\circ$  at the equator ( $N_e = 12$ ,  $N = 3$ ). The diffusion coefficient varies from  $\nu \text{ (m}^2 \text{ s}^{-1}) = 0, 10^2, 10^3, 10^4$ . All tests are integrated for 5 days with  $\Delta t = 90 \text{ s}$ .

4.3.1. To test the maintenance of well-balanced property

In order to verify that the models indeed maintain well-balanced property, we use a steady atmosphere over a smooth mountain (a Gaussian-hill), and a non-smooth mountain (a conical mountain, as (38)) respectively as a test case. To be specific, the steady atmosphere is given as,

$$u = 0, \quad v = 0, \quad h = h_0.$$

The Gaussian hill is chosen as [31],

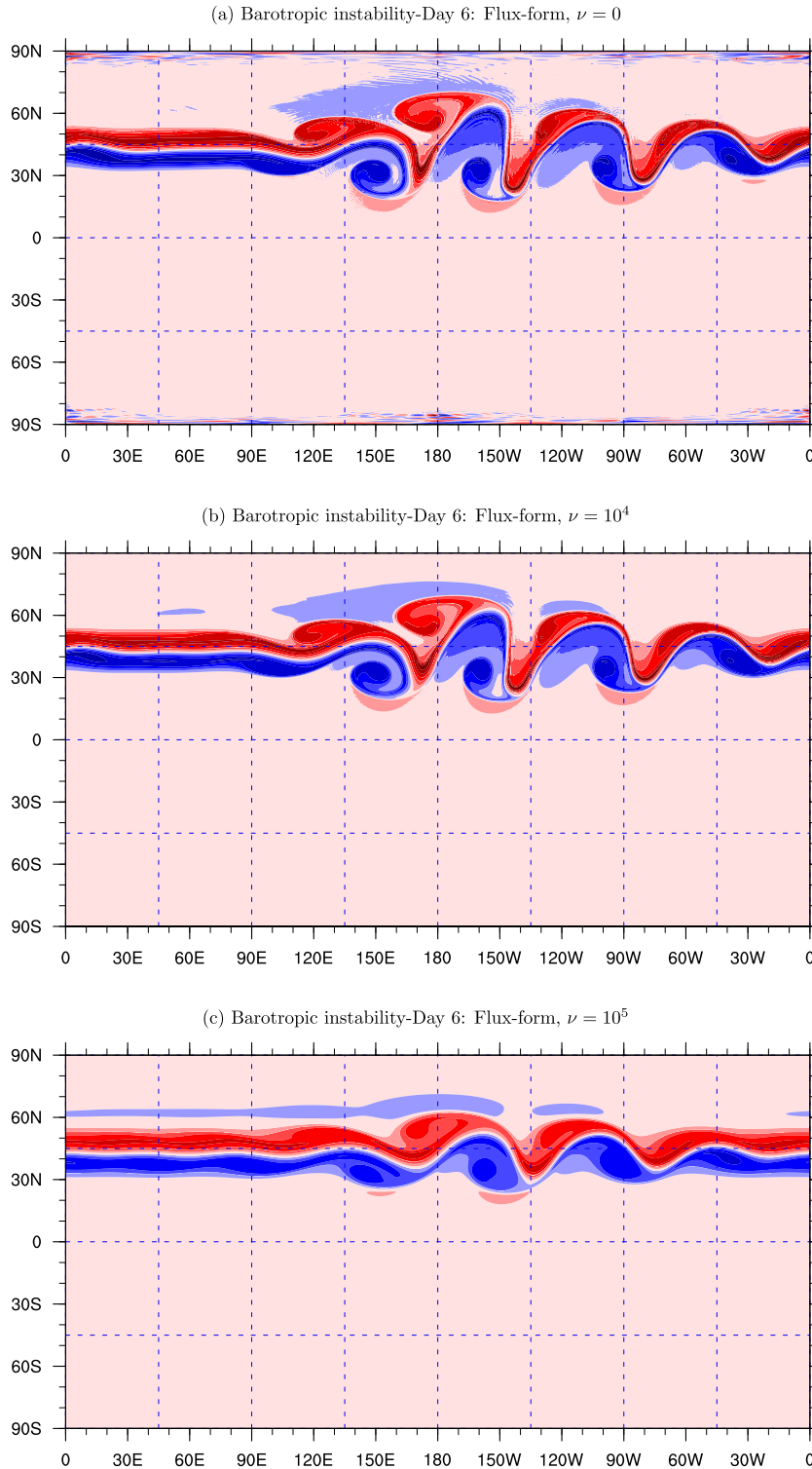


**Fig. 7.** Relative vorticity field of the barotropic instability test at day 6 in the resolution  $\approx 0.43^\circ$  at the equator ( $N_e = 30, N = 7$ ). (a) is using the inviscid flux-form. (b) is using the LDG flux-form with  $\nu = 10^4 \text{ m}^2 \text{ s}^{-1}$ . (c) is using the LDG flux-form with  $\nu = 10^5 \text{ m}^2 \text{ s}^{-1}$ .  $\Delta t = 5 \text{ s}$  for all runs. The contour varies from  $-1.1 \times 10^{-4} \text{ s}^{-1}$  to  $1.1 \times 10^{-4} \text{ s}^{-1}$  with an increment of  $2 \times 10^{-5} \text{ s}^{-1}$ .

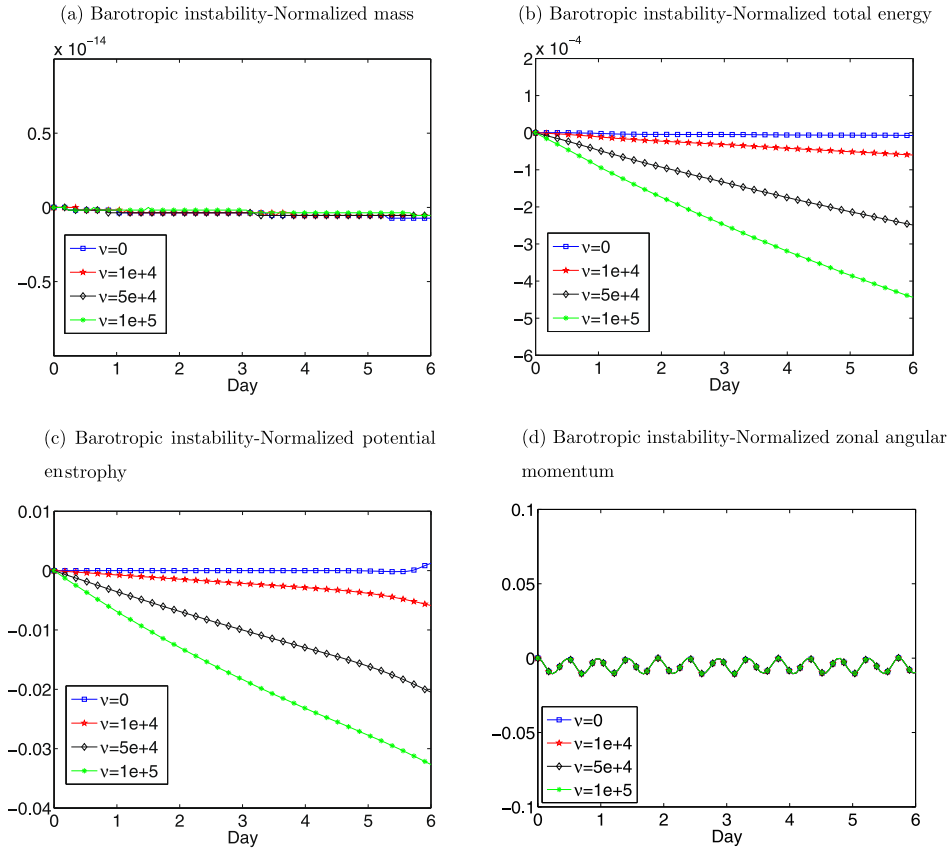


**Fig. 8.** Time traces of the normalized errors of mass (a), total energy (b), potential enstrophy (c) and zonal angular momentum (d) of LDG flux-form SW model for the barotropic instability test-case in the resolution  $\approx 1.5^\circ$  at the equator ( $N_e = 30, N = 7$ ). The diffusion coefficient  $\nu$  ( $m^2 s^{-1}$ ) varies from 0,  $10^4, 5 \times 10^4, 10^5$ . The tests are integrated for 6 days with  $\Delta t = 5$  s.

**Table 1**  
Well-balanced check for a steady flow field with a Gaussian smooth mountain.

SW DG model	$L^1$ error		$L^\infty$ error	
	$hu$	$hv$	$hu$	$hv$
V.I. form	1.61E-15	1.64E-15	1.74E-15	1.87E-15
flux-form	1.57E-13	1.58E-13	1.75E-12	1.74E-12

**Table 2**  
Well-balanced check for a steady flow field with a conical non-smooth mountain.

SW DG model	$L^1$ error		$L^\infty$ error	
	$hu$	$hv$	$hu$	$hv$
V.I. form	1.36E-15	1.42E-15	1.61E-15	1.61E-15
flux-form	1.54E-10	1.06E-10	3.32E-09	3.03E-09
well-balanced flux-form	1.99E-14	2.27E-14	4.44E-14	4.68E-14

$$h_s = h_s^0 \times \exp\{-5.0[(x - x_c)^2 + (y - y_c)^2 + (z - z_c)^2]\},$$

where  $(x, y, z)$  is the any point on the sphere and  $(x_c, y_c, z_c)$  is the point at  $(\lambda_c, \theta_c) = (3\pi/2, \pi/6)$ .

Table 1 and 2 show  $L_1$  and  $L_\infty$  error of the components of momentum of  $hu$  and  $hv$  under double precision for smooth bottom and non-smooth bottom, respectively. All numerical runs are integrated for 1 model day with  $N_e = 20, N = 3, \Delta t = 30$  sec. We can see that for the smooth mountain, both vector-invariant form and flux-form reach the roundoff error, which indicates the maintenance of the well-balanced property. However, for the non-smooth mountain, the vector-invariant form still preserves well-balanced property while the flux-form DG loses this property. After making the well-balanced correction to the flux-form, we can see that the flux-form DG keeps well-balanced property for the steady atmosphere.

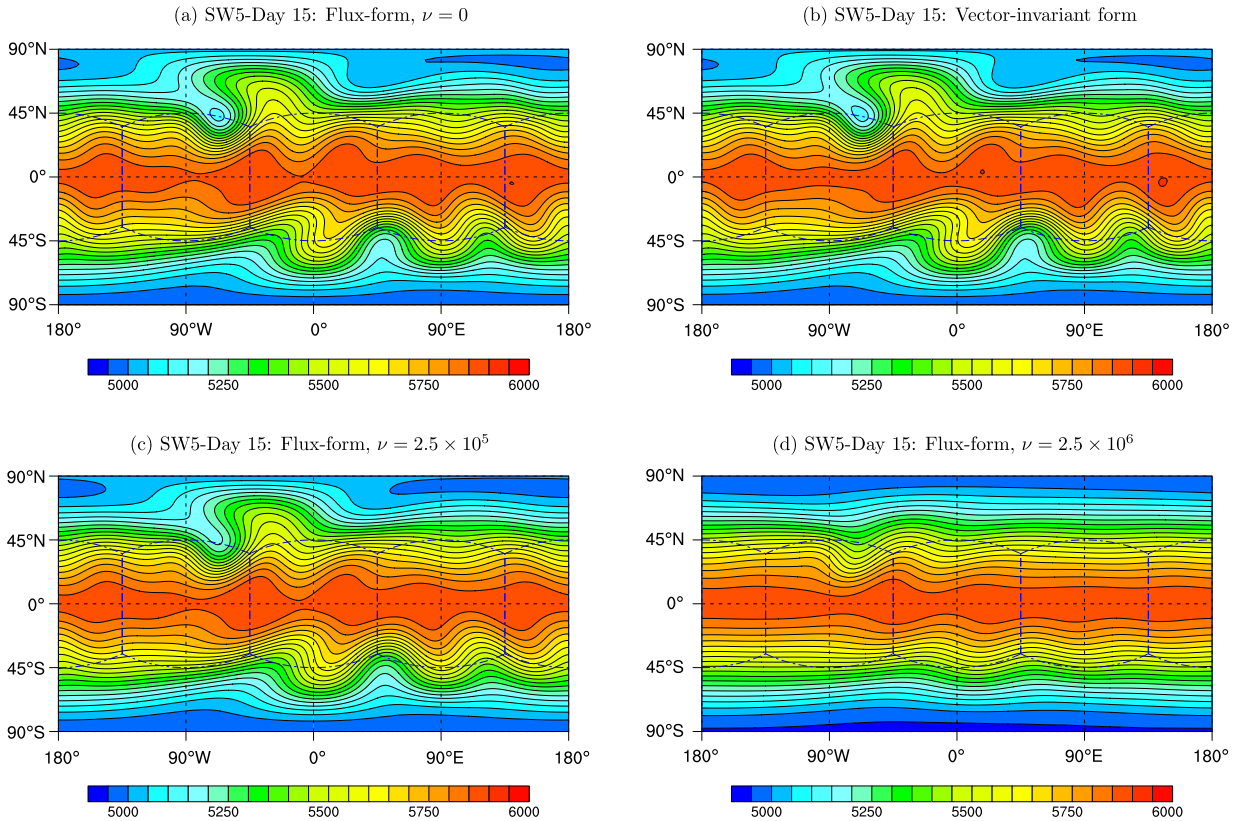


**Fig. 9.** Height field of the zonal flow over an isolated mountain wave (SW test-case 5) at day 15 in the resolution  $\approx 1.5^\circ$  at the equator ( $N_e = 20, N = 3$ ). (a) is using flux-form. (b) is using vector-invariant form. (c) is using LDG flux-form with  $\nu = 2.5 \times 10^5 \text{ m}^2 \text{ s}^{-1}$ . (d) is using LDG flux-form with  $\nu = 2.5 \times 10^6 \text{ m}^2 \text{ s}^{-1}$ .  $\Delta t = 30 \text{ s}$  for all tests.

#### 4.3.2. Inviscid DG of flux-form SWEs to SW test-case 5

This test-case is mainly designed for conservation check for the global invariants. Spectral elements and spectral transform suffer from the generation of spurious oscillations at all scales for this test problem, which leads to spectral ringings [14]. A 15 model days' time integration is performed for the zonal flow over an isolated mountain. The modal resolution is chosen to be  $N_e = 20, N = 3$ , which is approximately  $1.5^\circ$  at the equator. The time step size is  $\Delta t = 30 \text{ s}$  for all the numerical experiments. The height field at day 7 is shown in Fig. 9(a), and the result from vector-invariant form is plotted in Fig. 9(b) for reference. The results are visually indistinguishable and similar to the results in [14].

Time traces of the normalized errors of the conservative quantities: mass, total energy, potential enstrophy and angular momentum are shown in Fig. 10. In the non-diffusive case, both forms exhibit comparable performances on preserving the global invariants. In particular, the flux-form has a slightly better conservation of total energy and vector-invariant form shows a better conservation of potential enstrophy.

For the flux-form formulation, the influence of source term involving the non-smooth mountain can be readily seen in the vorticity fields. Although there are several global flux-form SW models [7,15,17,18] use this test-case, unfortunately, the vorticity fields are not available for a comparison. However, we examine the influence of diffusion mechanism in the evolution of relative vorticity fields, by comparing the vorticity fields at day 7 shown in Fig. 11. For the well-balanced DG without diffusion, as shown in Fig. 9(a), there exists some noise in the region where the mountain is located. Compared to the inviscid flux-form, the vector-invariant form produces a smooth relative vorticity field because the source term in (7) does not include the oscillatory gradient terms corresponding to the representation of the mountain  $h_s$ . The bottom mountain only exists in the flux term (6) and the discontinuity can be partially resolved by the numerical flux. However, it can be observed in Fig. 11(c), that the appropriate amount of diffusion effect can, to a great extent, eliminate the noise and the resulting vorticity field is very similar to the reference solution shown in Fig. 11(a). Fig. 11(d) shows an even smoother vorticity field at the cost of a higher diffusion, however, the corresponding height field shown in Fig. 9(d) is over-diffused.

#### 4.3.3. Well-balanced DG with numerical diffusion

To examine the influence of the diffusion effect on the maintenance of the conservative integrals, time traces of the normalized errors of mass, total energy, potential enstrophy and zonal angular momentum are shown in Fig. 12. Unlike the previous cases, the magnitude of normalized errors first decreases and then increases as the magnitude of the diffusion

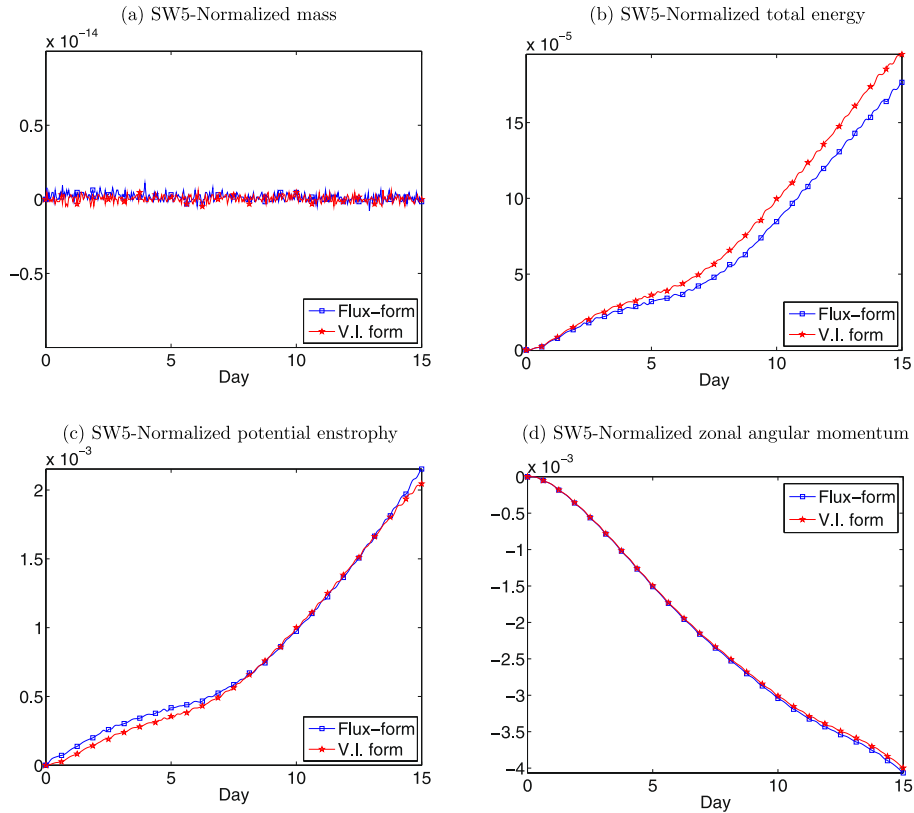


**Fig. 10.** Time traces of the normalized errors of (a) mass, (b) total energy, (c) potential enstrophy and (d) zonal angular momentum of two forms of SWEs for the zonal flow over an isolated mountain wave (SW test-case 5) in the resolution  $\approx 1.5^\circ$  at the equator ( $N_e = 20, N = 3$ ). Both tests are integrated for 15 days with  $\Delta t = 30$  s.

coefficient grows. This is mainly due to the fact that the inviscid flux-form generates some spurious vorticity near the mountain region and proper diffusion effect (here choose  $\nu = 2.5 \times 10^5 \text{ m}^2 \text{ s}^{-1}$ ) can suppress the noise in the relative vorticity field, as shown in Fig. 11(c). Further increase in the diffusion effect leads to an over-diffused state, which is not acceptable. So the conservative properties are further destroyed besides the effect from the numerical scheme itself. As the diffusion coefficient increases to  $2.5 \times 10^6 \text{ m}^2 \text{ s}^{-1}$ , the magnitude of the normalized error grows. However, a high-order diffusion ( $\nabla^{2n}$ ) can more efficiently remove the noise without adversely affecting the flow field [44], which is not considered here.

## 5. Summary and conclusion

A full flux-form discontinuous Galerkin (DG) shallow-water (SW) model on the cubed-sphere has been developed. The cubed-sphere is based on non-orthogonal curvilinear coordinates and uses equiangular central projection. To address the explicit non-smooth source terms in the momentum equations, the well-balanced DG scheme proposed by Xing et al. has been extended to the global SW model. The resulting DG discretization uses a high-order nodal basis set consisting of Lagrange–Legendre polynomials and adopts the Lax–Friedrichs numerical flux combined with the well-balanced flux modification. Time integration relies on a strong stability-preserving (SSP) explicit Runge–Kutta scheme. The viscous variant of the SW model employs a second-order diffusion scheme, which is based on the local discontinuous Galerkin (LDG) method. The diffusion terms (Laplacians) of the model involving curvilinear metric terms are solved via a first-order system. In order to demonstrate accuracy and conservation properties, we have tested the proposed model with a suite of SW test-cases, including two benchmark test-cases from Williamson et al. [2] and a barotropic instability test from Galewsky et al. [27]. The inviscid vector-invariant form SW model is used here as a reference. Our goal is to make a rigorous comparison of the two formulations of the SWEs, in terms of physical features such as conservation, for identifying a formulation that would be suitable for a global 3D dynamical-core development.

The accuracy of the inviscid flux-form DG SW model can be demonstrated by the exponential convergence of the SW steady state test-case (SW test-case 2, above). The numerical results are similar to the reference solution obtained via the vector-invariant form DG SW model. For the flux-form SW model, in the presence of a non-flat bottom topography, a special approach which preserves the “well-balanced property” is required. This essentially prevents the source terms in the DG discretization of the flux-form SWEs from exciting spurious modes. The results with a benchmark test, flow over

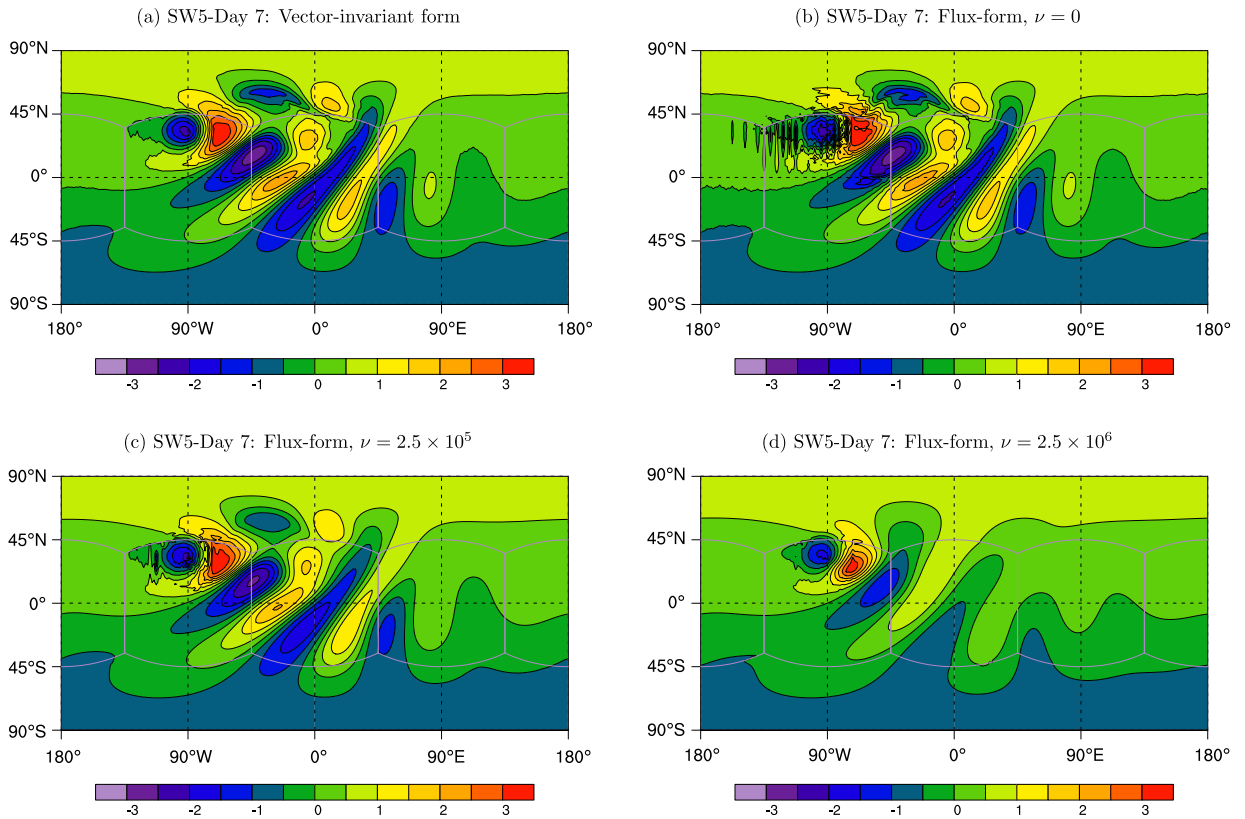


**Fig. 11.** Relative vorticity field of the zonal flow over an isolated mountain wave (SW test-case 5) at day 7 in the resolution  $\approx 1.5^\circ$  at the equator ( $N_e = 20, N = 3$ ). (a) is using inviscid flux-form and (b) is using vector-invariant form. (c) is using viscid flux-form with  $\nu = 2.5 \times 10^5 \text{ m}^2 \text{ s}^{-1}$ . (d) is using viscid flux-form with  $\nu = 2.5 \times 10^6 \text{ m}^2 \text{ s}^{-1}$ .  $\Delta t = 30 \text{ s}$  for all tests. The contour varies from  $-3 \times 10^{-5} \text{ s}^{-1}$  to  $3 \times 10^{-5} \text{ s}^{-1}$  with an increment of  $5 \times 10^{-6} \text{ s}^{-1}$ .

an isolated mountain (SW test-case 5), show that the vector-invariant formulation is well-balanced for both smooth and non-smooth mountains. The flux-form DG SW model is well-balanced for the smooth mountain case. But in the presence of non-smooth mountains, the well-balanced correction is necessary to admit the solution and prevent the spurious numerical behaviors. While monitoring the vorticity field, it is observed that the flux-form SW model generates spurious noise in the vicinity of the mountain, but this is not the case for the vector-invariant form. For the conservation of global invariants, the inviscid flux-form SW model shows better conservation of total energy and angular momentum while the vector-invariant form has a better control on the potential enstrophy.

The LDG scheme for the flux-form SWEs evolves to a diffused state for SW test-case 2, and this process is dependent on the magnitude of the diffusion coefficient  $\nu$ . For the barotropic instability test, the flux-form SW model combined with the LDG diffusion process produces a result which agrees well with the reference solution shown in Galewsky et al. [27]. This scheme successfully removes the spurious oscillations, and captures the dynamics of the mid-latitude stream. The resulting numerical solutions are smooth and comparable to other published results. The quality of the diffused solution is also influenced by the value of  $\nu$ . When considering the effectiveness of the LDG schemes in preserving globally conservative quantities, the normalized errors of the global invariants grow at a faster rate than the inviscid situation and the error growth rates are dependent on the choice of the diffusion coefficient. However, the choice of the diffusion coefficient is mesh-size and problem dependent, and our choice is arbitrary and heuristic.

The SW model has been implemented in the highly parallel efficient HOMME framework [41]. As far as the computational complexity is concerned, the vector-invariant form is simpler and more efficient. The explicit SSP-RK time integration used for our DG SW models has a restrictive time-step size limit. An implicit or semi-implicit time integration would be an effective candidate, and we are considering this option for future application. The flux-form SW model requires additional efforts to discretize the source terms due to the non-smooth mountains, although it may not be an issue for a 3D atmosphere model. This is because the mountains (topography) can be incorporated into the vertical coordinate system, such as the terrain-following coordinate system. This set of equations will probably avoid the requirement of the well-balanced DG discretization for the conservative form of the momentum equations, and that is an interesting topic for future study. In addition, with an appropriate value for  $\nu$ , high-order (or hyper-) diffusion might better preserve global invariants. A rigorous selection for  $\nu$  is possible by looking at the kinetic energy spectra, and this may be considered for future research.

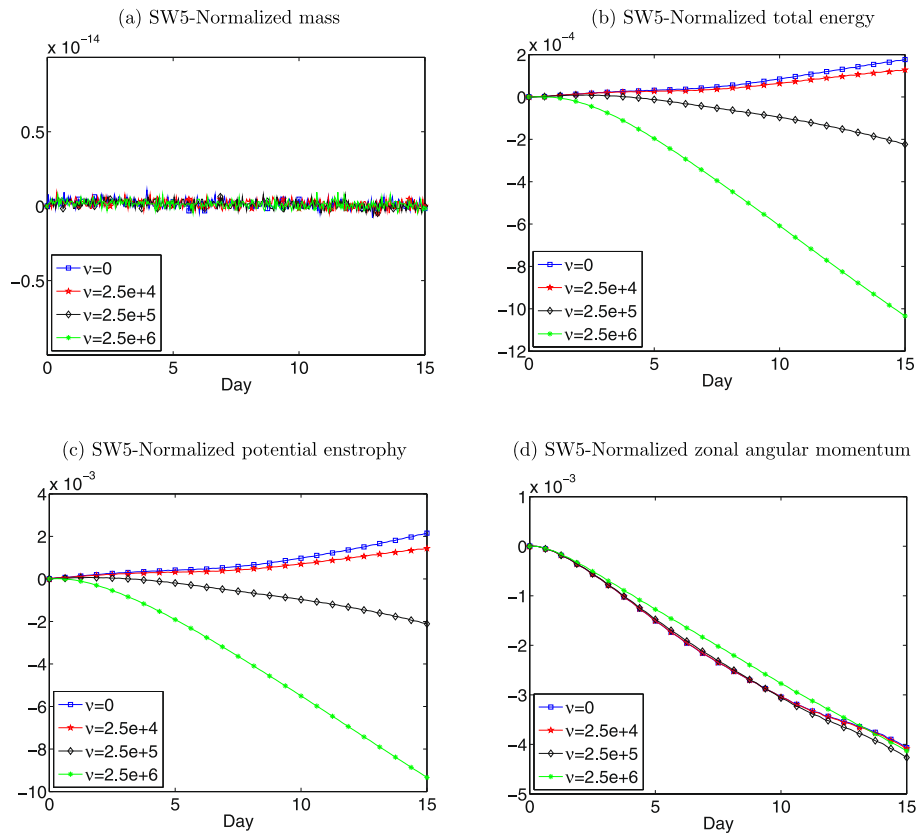


**Fig. 12.** Time traces of normalized errors of mass (a), total energy (b), potential enstrophy (c) and zonal angular momentum (d) of LDG flux-form SW model for the flow over a mountain (SW test-case 5) in the resolution  $\approx 1.5^\circ$  at the equator ( $N_e = 20, N = 3$ ). The diffusion coefficient varies from  $\nu$  ( $\text{m}^2 \text{s}^{-1}$ ) = 0,  $2.5 \times 10^4$ ,  $2.5 \times 10^5$ ,  $2.5 \times 10^6$ . All tests are integrated for 15 days with  $\Delta t = 30$  s.

## Acknowledgements

The authors thank Dr. Robert Klöforn (NCAR) for his assistance of parallel implementation of flux-form SWEs in HOMME and his careful review. The authors are grateful for Dr. David Hall and Tony Wong for the internal review. The authors would appreciate the anonymous reviewers, whose helpful comments and suggestions greatly improved the quality of the paper. The first author would like to thank IMAGE/NCAR for the support. This work was supported by the DOE BER Program under award DE-SC0006959.

## References

- [1] J. Pedlosky, *Geophysical Fluid Dynamics*, 2nd ed., Springer, 1987.
- [2] D.L. Williamson, J.B. Drake, J.J. Hack, R. Jakob, P.N. Swartztrauber, A standard test set for numerical approximations to the shallow water equations in spherical geometry, *J. Comput. Phys.* 102 (1) (1992) 211–224.
- [3] M. Beddhu, K.L. Taylor, D.L. Whitefield, Strong conservative form of incompressible Navier–Stokes equations in a rotating frame with a solution procedure, *J. Comput. Phys.* 128 (1996) 427–437.
- [4] J. Thuburn, Some conservation issues for the dynamical cores of NWP and climate models, *J. Comput. Phys.* 227 (7) (2008) 3715–3730.
- [5] T.D. Ringler, Momentum, vorticity and transport: considerations in the design of a finite-volume dynamical core, in: *Numerical Techniques for Global Atmospheric Models*, Springer, 2011, pp. 143–183.
- [6] J. Egger, K. Weickmann, K.-P. Hoinka, Angular momentum in the global atmospheric circulation, *Rev. Geophys.* 45 (4) (2007) RG4007.
- [7] F.X. Giraldo, J.S. Hesthaven, T. Warburton, Nodal high-order discontinuous Galerkin methods for the spherical shallow water equations, *J. Comput. Phys.* 181 (2) (2002) 499–525.
- [8] H. Weller, H.G. Weller, A. Fournier, Voronoi, Delaunay, and block-structured mesh refinement for solution of the shallow-water equations on the sphere, *Mon. Weather Rev.* 137 (2009) 4208–4224.
- [9] J. Côté, A Lagrange multiplier approach for the metric terms of semi-lagrangian models on the sphere, *Q. J. R. Meteorol. Soc.* 114 (1988) 1347–1352.
- [10] R. Sadourny, Conservative finite-difference approximations of the primitive equations on quasi-uniform spherical grids, *Mon. Weather Rev.* 100 (2) (1972) 136–144.
- [11] C. Ronchi, R. Iacono, P.S. Paolucci, The “Cubed Sphere”: a new method for the solution of partial differential equations in spherical geometry, *J. Comput. Phys.* 124 (1) (1996) 93–114.
- [12] M. Rančić, R.J. Purser, F. Mesinger, A global shallow-water model using an expanded spherical cube: Gnomonic versus conformal coordinates, *Q. J. R. Meteorol. Soc.* 122 (532) (1996) 959–982.

- [13] M. Taylor, J. Tribbia, M. Iskandarani, The spectral element method for the shallow water equations on the sphere, *J. Comput. Phys.* 130 (1) (1997) 92–108.
- [14] R.D. Nair, S.J. Thomas, R.D. Loft, A discontinuous Galerkin global shallow water model, *Mon. Weather Rev.* 133 (4) (2005) 876–888.
- [15] J.A. Rossmanith, A wave propagation method for hyperbolic systems on the sphere, *J. Comput. Phys.* 213 (2006) 629–658.
- [16] C. Chen, F. Xiao, Shallow water model on cubed-sphere by multi-moment finite volume method, *J. Comput. Phys.* 227 (2008) 5019–5044.
- [17] P.A. Ullrich, C. Jablonowski, B. van Leer, High-order finite-volume methods for the shallow-water equations on the sphere, *J. Comput. Phys.* 229 (2010) 6104–6134.
- [18] C. Yang, J. Cao, X.-C. Cai, A fully implicit domain decomposition algorithm for shallow water equations on the cubed-sphere, *SIAM J. Sci. Comput.* 32 (1) (2010) 418–438.
- [19] R.D. Nair, K.K. Katta, The central-upwind finite-volume method for atmospheric numerical modeling, *Contemp. Math.* 586 (2013) 277–285.
- [20] A.E. Gill, *Atmosphere–Ocean Dynamics*, International Geophysics Series, vol. 30, Academic Press, 1982.
- [21] B. Cockburn, An introduction to the Discontinuous-Galerkin method for convection-dominated problems, in: A. Quarteroni (Ed.), *Lecture Notes in Mathematics: Advanced Numerical Approximation of Nonlinear Hyperbolic Equations*, vol. 1697, Springer, 1997, pp. 151–268.
- [22] M. Läuter, F.X. Giraldo, D. Handorf, K. Dethloff, A discontinuous Galerkin method for the shallow water equations in spherical triangular coordinates, *J. Comput. Phys.* 227 (2008) 10226–10242.
- [23] R.D. Nair, Diffusion experiments with a global discontinuous Galerkin shallow-water model, *Mon. Weather Rev.* 137 (10) (2009) 3339–3350.
- [24] Y. Xing, C.-W. Shu, A new approach of high order well-balanced finite volume WENO schemes and discontinuous Galerkin methods for a class of hyperbolic systems with source terms, *Commun. Comput. Phys.* 1 (1) (2006) 100–134.
- [25] Y. Xing, X. Zhang, C.-W. Shu, Positivity-preserving high order well-balanced discontinuous Galerkin methods for the shallow water equations, *Adv. Water Resour.* 33 (12) (2010) 1476–1493.
- [26] S. Gottlieb, C.-W. Shu, E. Tadmor, Strong stability-preserving high-order time discretization methods, *SIAM Rev.* 43 (1) (2001) 89–112.
- [27] J. Galewsky, R.K. Scott, L.M. Polvani, An initial-value problem for testing numerical models of the global shallow-water equations, *Tellus A* 56 (5) (2004) 429–440.
- [28] E.F. Toro, *Shock-Capturing Methods for Free-Surface Shallow Flows*, Wiley, 2001.
- [29] R.D. Nair, S.J. Thomas, R.D. Loft, A discontinuous Galerkin transport scheme on the cubed sphere, *Mon. Weather Rev.* 123 (2005) 814–828.
- [30] C. Yang, X.-C. Cai, Parallel multilevel methods for implicit solution of shallow water equations with nonsmooth topography on the cubed-sphere, *J. Comput. Phys.* 230 (7) (2011) 2523–2539.
- [31] M.N. Levy, R.D. Nair, H.M. Tufo, High-order Galerkin methods for scalable global atmospheric models, *Comput. Geosci.* 33 (8) (2007) 1022–1035.
- [32] A. Bermudez, M.E. Vazquez, Upwind methods for hyperbolic conservation laws with source terms, *Comput. Fluids* 23 (8) (1994) 1049–1071.
- [33] S. Noelle, Y. Xing, C.-W. Shu, High-order well-balanced schemes, in: *Numerical Methods for Balance Laws*, Dept. Math., Seconda Univ. Napoli, Caserta, 2009, pp. 1–66.
- [34] B. Cockburn, C.-W. Shu, The local discontinuous Galerkin for convection diffusion systems, *SIAM J. Numer. Anal.* 35 (1998) 2440–2463.
- [35] F. Bassi, S. Rebay, A high-order accurate discontinuous finite element method for the numerical solution of the compressible Navier–Stokes equations, *J. Comput. Phys.* 131 (1997) 267–279.
- [36] D.N. Arnold, F. Brezzi, B. Cockburn, L.D. Marini, Unified analysis of discontinuous Galerkin methods for elliptic problems, *SIAM J. Numer. Anal.* 39 (5) (2002) 1749–1779.
- [37] N. Flyer, E. Lehto, S. Blaise, G.B. Wright, A. St-Cyr, A guide to RBF-generated finite differences for nonlinear transport: Shallow water simulations on a sphere, *J. Comput. Phys.* 231 (11) (2012) 4078–4095.
- [38] K.J. Evans, M.A. Taylor, J.B. Drake, Accuracy analysis of a spectral element atmospheric model using a fully implicit solution framework, *Mon. Weather Rev.* 138 (8) (2010) 3333–3341.
- [39] C. Jablonowski, D.L. Williamson, The pros and cons of diffusion, filters and fixers in atmospheric general circulation models, in: *Numerical Techniques for Global Atmospheric Models*, Springer, 2011, pp. 381–493.
- [40] M.A. Taylor, J. Edwards, S. Thomas, R. Nair, A mass and energy conserving spectral element atmospheric dynamical core on the cubed-sphere grid, *J. Phys. Conf. Ser.* 78 (1) (2007) 012074.
- [41] R.D. Nair, H.-W. Choi, H.M. Tufo, Computational aspects of a scalable high-order discontinuous Galerkin atmospheric dynamical core, *Comput. Fluids* 38 (2009) 309–319.
- [42] M. Satoh, *Atmospheric Circulation Dynamics and Circulation Models*, Springer Verlag, 2004.
- [43] A. St-Cyr, C. Jablonowski, J.M. Dennis, H.M. Tufo, S.J. Thomas, A comparison of two shallow-water models with nonconforming adaptive grids, *Mon. Weather Rev.* 136 (2008) 1898–1922.
- [44] A. Gelb, J.P. Gleeson, Spectral viscosity for shallow water equations in spherical geometry, *Mon. Weather Rev.* 129 (2001) 2346–2360.